

# Diffusion of tangential tensor fields: numerical issues and influence of geometric properties

E. Bachini<sup>1</sup>, P. Brandner<sup>2</sup>, T. Jankuhn<sup>2</sup>, M. Nestler<sup>1</sup>,  
S. Praetorius<sup>\*1</sup>, A. Reusken<sup>2</sup>, and A. Voigt<sup>1</sup>

<sup>1</sup>*Institut für Wissenschaftliches Rechnen, Technische Universität Dresden, D-01062 Dresden, Germany.*

<sup>2</sup>*Institut für Geometrie und Praktische Mathematik, RWTH Aachen University, D-52056 Aachen, Germany*

**Abstract.** We study the diffusion of tangential tensor-valued data on curved surfaces. For this several finite element based numerical methods are collected and used to solve a tangential surface  $n$ -tensor heat flow problem. These methods differ with respect to the surface representation used, the required geometric information and the treatment of the tangentiality condition. We highlight the importance of geometric properties and their increasing influence if the tensorial degree changes from  $n = 0$  to  $n \geq 1$ . A specific example is presented that illustrates how curvature drastically affects the behavior of the solution.

**Keywords.** finite elements, surface heat equation, tangential tensor fields

## 1 Introduction

The Isaac Newton Institute programme “Computational challenges in partial differential equations” in 2003 stimulated intense research on surface partial differential equations (PDEs) in the mathematical community covering topics from modeling, numerical analysis, and applications. PDEs that are defined on curved surfaces are intrinsically nonlinear and require a geometric framework. An important breakthrough in the development of numerical methods for this type of PDEs is the avoidance of charts and atlases. Most commonly used methods are either based on a triangulated surface and require geometric information through knowledge of the vertices and discrete normals, or based on a level set technique in which geometric information is derived from the level set function. Most of that work is concerned with scalar-valued surface PDEs, see [9, 22, 2] for reviews on

---

\*Corresponding author: [simon.praetorius@tu-dresden.de](mailto:simon.praetorius@tu-dresden.de)

May 26, 2022

such finite element based approaches. In the scalar case the coupling between surface geometry and the PDE solution is relatively weak, and numerical approaches developed for PDEs in a flat space need only minor modifications to be applicable to surface equations, see, e.g., [9, 29]. For  $n$ -tensor-valued surface PDEs with  $n \geq 1$ , these approaches are not directly applicable. The tensor-fields then need to be considered as elements of the tangent bundle and the surface derivatives require more geometric information. This leads to a stronger influence of the surface geometry on the solution of the PDE.

In this paper we study in more depth this change in numerical complexity when going from PDEs in flat domains to curved surfaces. For this we consider a specific problem class, namely that of a surface heat equation for  $n$ -tensor fields on a smooth curved surface embedded in  $\mathbb{R}^3$ . We will focus on tensor ranks  $n = 0, 1, 2$ . In the remainder of the paper we use for  $n$ -tensors,  $n = 0, 1, 2$ , the terminology scalars, vectors and tensors, respectively. For  $n = 1, 2$ , the solution must be tangential. Concerning the numerics we restrict to finite element discretizations in space combined with low order BDF time stepping schemes, cf. [19]. When going from PDEs in flat Euclidean domains to PDEs on a curved surface the following additional numerical issues arise:

- a) *Surface representation.* In flat domains one only has to represent or approximate the boundary of the computational domain. In problems on curved surfaces the whole computational domain has to be approximated. An issue directly related to this is the quadrature used in the finite element method.
- b) *Representation of the gradient operator and geometry information.* For the (co-variant) surface gradient operator different natural representations are available, leading to different numerical approaches. In the discretization process one needs approximations of geometric quantities such as surface normals and curvature. We will see that the geometric information needed depends on the gradient operator representation used and on the tensorial degree  $n$ .
- c) *Tangentiality condition.* For  $n$ -tensor fields with  $n \geq 1$  one has to take into account the condition that the solution must be tangential.

In recent years several approaches for dealing with these issues have been developed, leading to different numerical discretization methods. *We present, in a unified framework, four methods known from the literature and explicitly address the different approaches these methods use regarding a)–c).* These four methods are: A surface finite element method (SFEM) [20, 21, 13, 14], which extends the SFEM for scalar-valued surface PDEs [9, 8] to tensor-valued surface PDEs; an intrinsic surface finite element method (ISFEM), which so far has only been considered for scalar-valued surface PDEs [1]; a trace finite element method (TraceFEM) [15], extending the scalar version [22] to vector-valued PDEs; and a diffuse interface approach (DI) [20] which extends the approach for scalar-valued PDEs [23]. We note that for vector- or tensor-valued surface PDEs only very few rigorous discretization error analyses are available. Such analyses for SFEM and TraceFEM applied to a vector-Laplace problem are given in [13, 15, 14].

One conclusion from this comparative study is that in all four methods there is *an essential increase in numerical complexity when one goes from the scalar case to the*

*vector- or tensor-valued problem*, which goes well beyond the increase in complexity in flat Euclidean domains. Depending on the geometry, an approximation of geometric properties, which is sufficient to achieve the desired accuracy of the solution for the scalar case, might fail for the vector or tensor case, cf. Section 3.5 for a further discussion.

We further consider the *influence of the geometry on the solution of an  $n$ -tensor heat flow problem*. This is done on a surface with a rather simple geometry. We present results of numerical simulations with the four methods which demonstrate that curvature drastically affects the behaviour of the solution.

The paper is structured as follows: In Section 2 we recall different surface representations. We also discuss different possibilities for representing tensors and gradient operators. Furthermore, we introduce the surface  $n$ -tensor-valued heat equation and summarize known analytical results. In Section 3 we briefly describe the four numerical methods and discuss the above mentioned numerical issues a)–c). In Section 4 the  $n$ -tensor-valued heat equation is numerically solved on a specific surface. Certain influences of the geometry on the behavior of the solution are addressed in the Sections 4.2 – 4.4.

Below we restrict to tensorial degree  $n \leq 2$ . This restriction is not essential for the results presented or for the applicability of the numerical methods, but allows a clearer presentation. We provide reference solutions, which can serve as a benchmark problem.

## 2 Surface tensor diffusion

### 2.1 Surface representation

Let  $\mathcal{M}$  be a compact, orientable, two-dimensional surface isometrically embedded into  $\mathbb{R}^3$ . We consider two representations of this surface, namely based on a local parametrization and as the zero level of a level set function. The tangent bundle of  $\mathcal{M}$  is denoted by  $\mathbb{T}\mathcal{M}$  and for each  $\mathbf{x} \in \mathcal{M}$  a normal vector  $\mathbf{n}(\mathbf{x}) \in \mathbb{R}^3$  is defined as the unit vector orthogonal to all tangent vectors in  $\mathbb{T}_{\mathbf{x}}\mathcal{M}$ .

#### 2.1.1 Parameterized surface

We assume that  $\mathcal{M}$  can be covered by a  $C^k$ -atlas  $\{(\boldsymbol{\mu}_r, \hat{\Omega}_r, U_r)\}_r$  of bijective mappings  $\boldsymbol{\mu}_r: \hat{\Omega}_r \rightarrow U_r \cap \mathcal{M}$  that are charts of class  $C^k$  with the domain open subsets  $\hat{\Omega}_r \subset \mathbb{R}^2$ . We further assume that the transition maps  $\boldsymbol{\mu}_r^{-1} \circ \boldsymbol{\mu}_s$  between overlapping co-domains,  $\boldsymbol{\mu}_r(\hat{\Omega}_r) \cap \boldsymbol{\mu}_s(\hat{\Omega}_s) \neq \emptyset$ , are  $C^k$ -diffeomorphisms.

For a local parametrization  $\boldsymbol{\mu} = \boldsymbol{\mu}_r$  we denote by  $\mathbf{x} = \boldsymbol{\mu}(\hat{\mathbf{x}}) \in \mathcal{M}$  the surface coordinate associated to the local coordinate  $\hat{\mathbf{x}} = (\hat{x}^1, \hat{x}^2) \in \hat{\Omega} = \hat{\Omega}_r$ ,

$$[\mathbf{J}(\mathbf{x})]_{ij} := [\hat{\nabla}\boldsymbol{\mu}(\hat{\mathbf{x}})]_{ij} = \frac{\partial \mu^i}{\partial \hat{x}^j}(\hat{\mathbf{x}}), \quad i = 1, 2, 3; j = 1, 2,$$

the Jacobian of the parametrization, and  $\mathbf{g} = \mathbf{J}^T \mathbf{J}$  the surface metric tensor. The columns of  $\mathbf{J}$  are tangential to  $\mathcal{M}$ , i.e.,  $\mathbf{t}_j(\mathbf{x}) := \mathbf{J}(\mathbf{x})_{:,j} \in \mathbb{T}_{\mathbf{x}}\mathcal{M}$  for  $j = 1, 2$ , with

$\mathbf{x} = \boldsymbol{\mu}(\hat{\mathbf{x}})$ . This gives rise to the definition of the normal direction  $\mathbf{m} = \mathbf{t}_1 \times \mathbf{t}_2$  and corresponding unit normal field  $\mathbf{n} = \mathbf{m}/\|\mathbf{m}\|$ .

A regular  $C^2$ -surface has an invertible metric. This allows to transform derivatives from the parameter domain  $\hat{\Omega}$  into surface derivatives, cf. Section 2.2.1. The Weingarten map is given by

$$[\mathbf{H}(\mathbf{x})]_{ij} := -J_{jk} g^{kl} \frac{\partial n^i}{\partial \hat{x}^l}(\hat{\mathbf{x}}),$$

where  $\mathbf{g}^{-1} = [g^{ij}]$  is the inverse of the metric tensor. Here and in the remainder we use the Einstein summation convention.

### 2.1.2 Level set characterization of the surface

An implicit representation of  $\mathcal{M}$  can be based on a  $C^k$ -mapping  $\phi: \Omega \rightarrow \mathbb{R}$  with  $\mathcal{M} \subset \Omega \subset \mathbb{R}^3$  a three-dimensional domain containing the surface. We assume that  $\nabla\phi \neq 0$  on  $\mathcal{M}$  and represent the surface as the zero-level set of  $\phi$ :

$$\mathcal{M} = \{\mathbf{x} \in \Omega \mid \phi(\mathbf{x}) = 0\}.$$

In a sufficiently small  $\delta$ -neighborhood  $U_\delta(\mathcal{M}) \subset \mathbb{R}^3$  of  $\mathcal{M}$  we can define the normal direction  $\bar{\mathbf{m}}(\mathbf{x}) = \nabla\phi(\mathbf{x})$ ,  $\mathbf{x} \in U_\delta(\mathcal{M})$ , and normal field  $\bar{\mathbf{n}}_\phi = \bar{\mathbf{m}}/\|\bar{\mathbf{m}}\|$  with  $\bar{\mathbf{n}}_\phi|_{\mathcal{M}} = \mathbf{n}$ . Here and in the remainder we use an overline notation, e.g.,  $\bar{\mathbf{m}}$ , to denote quantities that are defined not only on  $\mathcal{M}$  but in a (small) three-dimensional neighborhood of  $\mathcal{M}$ .

A natural choice for  $\phi$  would be the signed-distance function  $\rho(\mathbf{x}) = \text{dist}(\mathbf{x}, \mathcal{M})$  with the property  $\|\nabla\rho\| \equiv 1$ . Let  $\delta > 0$  be sufficiently small so that the closest-point projection  $\pi: U_\delta(\mathcal{M}) \rightarrow \mathcal{M}$  is uniquely defined by

$$\pi(\mathbf{x}) := \mathbf{x} - \rho(\mathbf{x})\mathbf{n}(\pi(\mathbf{x})), \quad \mathbf{x} \in U_\delta(\mathcal{M}). \quad (1)$$

Using the closest-point projection the signed-distance function can be determined based on  $\rho(\mathbf{x}) = (\mathbf{x} - \pi(\mathbf{x})) \cdot \mathbf{n}(\pi(\mathbf{x}))$ . The normal field  $\bar{\mathbf{n}}(\mathbf{x}) = \nabla\rho(\mathbf{x})$ ,  $\mathbf{x} \in U_\delta(\mathcal{M})$ , is a constant extension of the surface normal, i.e.,  $\bar{\mathbf{n}}(\mathbf{x}) = \mathbf{n}(\pi(\mathbf{x}))$ . An alternative representation of the extended Weingarten map is given by  $\bar{\mathbf{H}}(\mathbf{x}) = -\nabla\bar{\mathbf{n}}(\mathbf{x}) = -\nabla^2\rho(\mathbf{x})$ , for  $\mathbf{x} \in U_\delta(\mathcal{M})$  with  $\bar{\mathbf{H}}|_{\mathcal{M}} = \mathbf{H}$ .

## 2.2 Representation of tensor fields and gradient operators

### 2.2.1 Intrinsic representation

Starting from the definition of a parameterized surface, one can represent tensor fields and define derivatives making use of local coordinates in a reference domain  $\hat{\Omega}$ .

One possibility for the choice of the local coordinates is to consider the tangent vectors  $\mathbf{t}_1, \mathbf{t}_2$ , naturally associated with the parametrization  $\boldsymbol{\mu}$ , as reference frame for the tangent plane  $T_{\mathbf{x}}\mathcal{M}$ . We can then describe a function on  $\mathcal{M}$  in the local coordinates and define the (intrinsic) surface gradients. Let  $\mathbf{u}^{(0)}: \mathcal{M} \rightarrow \mathbb{R}$  be a scalar differentiable function on  $\mathcal{M}$ ,  $\mathbf{u}^{(1)}: \mathcal{M} \rightarrow T\mathcal{M}$  a tangent vector field given by  $\mathbf{u}^{(1)} = u^1\mathbf{t}_1 + u^2\mathbf{t}_2 = u^i\mathbf{t}_i$ , and  $\mathbf{u}^{(2)}: \mathcal{M} \rightarrow T^2\mathcal{M}$  a tangent tensor field given by  $\mathbf{u}^{(2)} = u^{ij}\mathbf{t}_i \otimes \mathbf{t}_j$ . At a point  $\mathbf{x} \in \mathcal{M}$ ,

the tensors of the contravariant components are denoted using underline notation, i.e.,  $\underline{\mathbf{u}}^{(0)} = u \in \mathbb{R}$ ,  $\underline{\mathbf{u}}^{(1)} = [u^i] \in \mathbb{R}^2$ , and  $\underline{\mathbf{u}}^{(2)} = [u^{ij}] \in \mathbb{R}^{2 \times 2}$ . The intrinsic gradient of an  $n$ -tensor field is an  $(n+1)$ -tensor field and is defined by the following expressions in terms of the contravariant components:

$$\left[ \nabla_{\mathcal{M}} \underline{\mathbf{u}}^{(0)} \right]^i = g^{il} \frac{\partial u}{\partial \hat{x}^l}, \quad (2)$$

$$\left[ \nabla_{\mathcal{M}} \underline{\mathbf{u}}^{(1)} \right]^{ij} = g^{il} \nabla_l u^j = g^{il} \left( \frac{\partial u^j}{\partial \hat{x}^l} + \Gamma_{lk}^j u^k \right), \quad (3)$$

$$\left[ \nabla_{\mathcal{M}} \underline{\mathbf{u}}^{(2)} \right]^{ijk} = g^{il} \nabla_l u^{jk} = g^{il} \left( \frac{\partial u^{jk}}{\partial \hat{x}^l} + \Gamma_{lh}^j u^{hk} + \Gamma_{lh}^k u^{jh} \right), \quad (4)$$

where  $\Gamma_{ij}^k = g^{kl} \mathbf{t}_l \cdot \frac{\partial \mathbf{t}_i}{\partial \hat{x}^j}$  denote the Christoffel symbols, for  $i, j, k = 1, 2$ . Note that these contain curvature information. Scalar products of tensors are explicitly written in terms of the metric  $\mathbf{g}$ , e.g.,

$$\langle \underline{\mathbf{u}}^{(1)}, \underline{\mathbf{v}}^{(1)} \rangle_{\mathbf{g}} := u^i v_i = g_{ij} u^i v^j, \quad \langle \underline{\mathbf{u}}^{(2)}, \underline{\mathbf{v}}^{(2)} \rangle_{\mathbf{g}} := u^{ij} v_{ij} = g_{il} g_{jm} u^{ij} v^{lm}.$$

To simplify the computation and to increase numerical stability, we also consider an orthogonal reference frame as basis for the tangent plane  $T_{\mathbf{x}} \mathcal{M}$ . For this we orthogonalize the vector  $\mathbf{t}_2$  with respect to  $\mathbf{t}_1$ . This orthogonalization yields the orthogonal frame  $\tilde{\mathbf{t}}_1, \tilde{\mathbf{t}}_2$  on  $T_{\mathbf{x}} \mathcal{M}$ , associated to the local coordinates  $\hat{\mathbf{s}} = (\hat{s}^1, \hat{s}^2)$ . The corresponding metric tensor is given by

$$\tilde{\mathbf{g}} := \begin{pmatrix} \|\tilde{\mathbf{t}}_1\|^2 & 0 \\ 0 & \|\tilde{\mathbf{t}}_2\|^2 \end{pmatrix} =: \begin{pmatrix} h_{(1)}^2 & 0 \\ 0 & h_{(2)}^2 \end{pmatrix}.$$

We can now write explicit expressions for the Christoffel symbols in the basis  $\{\tilde{\mathbf{t}}_1, \tilde{\mathbf{t}}_2\}$ :

$$\Gamma_{ik}^k = \Gamma_{ki}^k = \frac{1}{h_{(k)}} \frac{\partial h_{(k)}}{\partial \hat{s}^i} \quad i, k = 1, 2, \quad \Gamma_{ii}^k = -\frac{h_{(i)}}{h_{(k)}^2} \frac{\partial h_{(i)}}{\partial \hat{s}^k} \quad i \neq k, \quad (5)$$

$$\Gamma_{ij}^k = 0 \quad i \neq j \neq k, \quad (6)$$

which are simplified due to the orthogonality property. Also the scalar products simplify with the metric  $\tilde{\mathbf{g}}$ , e.g.,  $\langle \underline{\mathbf{u}}^{(2)}, \underline{\mathbf{v}}^{(2)} \rangle_{\tilde{\mathbf{g}}} = \tilde{g}_{il} \tilde{g}_{jm} u^{ij} v^{lm} = h_{(i)}^2 h_{(j)}^2 u^{ij} v^{ij}$ .

### 2.2.2 Representation based on embedding

An alternative convenient representation, to be used in SFEM, TraceFEM, and DI, follows from considering the  $n$ -tensor fields as general mappings into the embedding space, e.g.,

$$\underline{\mathbf{u}}^{(0)}: \mathcal{M} \rightarrow \mathbb{R}, \quad \underline{\mathbf{u}}^{(1)}: \mathcal{M} \rightarrow \mathbb{R}^3, \quad \underline{\mathbf{u}}^{(2)}: \mathcal{M} \rightarrow L(\mathbb{R}^3, \mathbb{R}^3). \quad (7)$$

If in  $\mathbb{R}^3$  we use the standard basis, then the component vector  $\underline{\mathbf{u}}^{(n)}$ ,  $n = 1, 2$ , can be identified with the corresponding fields  $\mathbf{u}^{(n)}$ . To simplify the notation, we use this

identification and delete the underline in the notation of the tensor fields if the meaning is clear from the context. This embedded representation gives rise to a natural inner product defined in the embedding, i.e., for  $n$ -tensors  $\underline{\mathbf{u}}^{(n)} := [u^{j_1 \dots j_n}]$  and  $\underline{\mathbf{v}}^{(n)} := [v^{j_1 \dots j_n}]$ , we have

$$\langle \underline{\mathbf{u}}^{(n)}, \underline{\mathbf{v}}^{(n)} \rangle := u^{j_1 \dots j_n} v_{j_1 \dots j_n},$$

where rising and lowering of indices can be done using the Euclidean metric  $\delta_{ij}$ . Note that since the tensor fields are represented in the embedding space, the indices are in the range  $j_k \in \{1, 2, 3\}$ .

Corresponding to the unit normal field  $\mathbf{n}$  we introduce the tangential projection  $\mathbf{P} = \mathbf{I} - \mathbf{n} \otimes \mathbf{n}$  and denote in the following a general tensor projection operator for  $n$ -tensors  $\underline{\mathbf{u}}^{(n)} = [u^{j_1 \dots j_n}]$  as  $\mathcal{P}$ , defined by componentwise projection,

$$[\mathcal{P}\underline{\mathbf{u}}^{(n)}]^{i_1 \dots i_n} := P^{i_1}_{j_1} \dots P^{i_n}_{j_n} u^{j_1 \dots j_n}. \quad (8)$$

The (total) covariant derivative of tangential tensor fields  $\underline{\mathbf{u}}^{(n)}$  with embedded representation  $\underline{\mathbf{u}}^{(n)}$  can be defined as  $\nabla_{\mathcal{M}}\underline{\mathbf{u}}^{(n)} := \mathcal{P}\nabla\bar{\underline{\mathbf{u}}}^{(n)}$ . Recall that the overline symbol denotes a (smooth) extension of a function to a surface neighborhood, whereas the underline symbol highlights that the Euclidean gradient  $\nabla$  is applied componentwise. Written out for  $n = 0, 1, 2$ , this definition reads:

$$\nabla_{\mathcal{M}}\mathbf{u}^{(0)} = \mathbf{P}\nabla\bar{\mathbf{u}}^{(0)}, \quad (9)$$

$$\nabla_{\mathcal{M}}\mathbf{u}^{(1)} = \mathbf{P}\nabla\bar{\mathbf{u}}^{(1)}\mathbf{P}, \quad (10)$$

$$\left[ \nabla_{\mathcal{M}}\mathbf{u}^{(2)} \right]^{i_1 i_2 i_3} = P^{i_1}_{j_1} P^{i_2}_{j_2} P^{i_3}_{j_3} \frac{\partial \bar{u}^{j_1 j_2}}{\partial x^{j_3}}. \quad (11)$$

The definitions in (9) and (2) yield the same surface gradient operator for scalar functions. The definitions in (10) and (11) are used also for vector and tensor fields that are not in the tangent bundle. For the case that these fields are tangential, these definitions yield the same gradient operators as the ones defined in (3) and (4).

The divergence of a tangential  $n$ -tensor,  $n \geq 1$ , is given by

$$\left[ \operatorname{div}_{\mathcal{M}} \underline{\mathbf{u}}^{(n)} \right]^{i_1 \dots i_{n-1}} = P^{i_1}_{j_1} \dots P^{i_{n-1}}_{j_{n-1}} P_{i_n j_n} \frac{\partial \bar{u}^{j_1 \dots j_n}}{\partial x^{i_n}}. \quad (12)$$

### 2.3 Problem definition

We study the following model problem: Find tangential  $n$ -tensor fields  $\mathbf{u}$  that solve

$$\partial_t \mathbf{u} - \Delta_{\mathcal{M}} \mathbf{u} = 0 \quad \text{on } \mathcal{M}, \quad (13)$$

subject to appropriate ‘‘no-flux’’ boundary conditions and initial conditions. Note that for  $n = 0$  the tangential condition is void. For  $n \geq 1$ , the  $\Delta_{\mathcal{M}}$  operator is the (negative) connection-Laplacian, the natural extension of the Laplace-Beltrami operator to  $n$ -tensor fields. It can be written as  $\Delta_{\mathcal{M}} \mathbf{u} = \operatorname{div}_{\mathcal{M}} \nabla_{\mathcal{M}} \mathbf{u}$ , with  $\nabla_{\mathcal{M}}$  the covariant gradient operator defined above and  $\operatorname{div}_{\mathcal{M}}$  the tensor surface divergence as in (12).

For  $n = 0$  the PDE (13) corresponds to the scalar heat diffusion problem on a surface, which shares several properties with the corresponding equation in flat space. For instance, it holds that  $\langle \mathbf{u} \rangle(t) = \langle \mathbf{u}^0 \rangle$  and  $\mathbf{u}(t, \mathbf{x}) \rightarrow \langle \mathbf{u}^0 \rangle$  for  $t \rightarrow \infty$ , with the average  $\langle \mathbf{u} \rangle(t) = \frac{1}{\text{area}(\mathcal{M})} \int_{\mathcal{M}} \mathbf{u}(t, \mathbf{x}) d\mathbf{x}$  of  $\mathbf{u}(t, \mathbf{x})$ . It also holds that if  $\mathbf{u}^0 \geq 0$  on  $\mathcal{M}$  and  $\mathbf{u}^0 \not\equiv 0$ , then  $\mathbf{u}(t) > 0$  on  $\mathcal{M}$  for  $t > 0$ , see, e.g., [4]. There are also results available that explain certain influences of surface curvature on the solution of the scalar heat equation problem. We outline a few of such results. Let  $\mathbf{u}^0(\mathbf{x}) = \delta_{\mathbf{p}}(\mathbf{x})$  for some  $\mathbf{p} \in \mathcal{M}$  be the Dirac delta function. In [28] it is shown that for this initial condition the corresponding solution satisfies

$$\lim_{t \rightarrow 0} [-2t \log \mathbf{u}(t, \mathbf{x})] = d_{\mathcal{M}}^2(\mathbf{x}, \mathbf{p}),$$

with  $d_{\mathcal{M}}(\cdot, \cdot)$  the geodesic distance on  $\mathcal{M}$ . This property is used to approximate geodesic distances on curved surfaces in computer science [7]. In [10] the scalar heat equation is considered and rewritten in terms of geodesic polar coordinates. This allows to separate the diffusion from the geometric influence, with the last completely determined by the Gaussian curvature  $K$ . We now outline a result that will be used to explain a certain phenomenon observed in the numerical experiments in Section 4. The solution of the scalar heat equation with initial condition  $\delta_{\mathbf{p}}$  can be expressed as

$$\mathbf{u}(t, \mathbf{x}) = \int_{\mathcal{M}} k_t(\mathbf{x}, \mathbf{y}) \delta_{\mathbf{p}}(\mathbf{y}) d\mathbf{y} \quad (14)$$

with heat kernel  $k_t(\cdot, \cdot)$ . In [27, 12] it is shown that

$$k_t(\mathbf{x}, \mathbf{x}) = \frac{1}{4\pi t} \left( 1 + \frac{1}{6} K(\mathbf{x}) t + \text{h.o.}(t) \right). \quad (15)$$

This result motivates general statements like “heat tends to diffuse slower at points with positive curvature, and faster at points with negative curvature”. Also several analytical solutions of the heat equation for special surfaces have been derived [10].

For  $n = 1$ , the surface vector heat equation, some of these results can be generalized. In particular, it can be shown, again by considering the associated heat kernel, that for  $t \rightarrow 0$  it behaves like parallel transport along geodesics, along with a decay in magnitude that is identical to the decay of the scalar heat kernel [24]. This property is crucial for various applications in computer graphics [16, 24] and data science [25], where it is also extended to tensor fields with  $n > 1$ . As the tangential tensor-valued heat equation can also be considered as the  $L^2$ -gradient flow for the tensor Dirichlet energy  $\int_{\mathcal{M}} \|\nabla_{\mathcal{M}} \mathbf{u}\|^2 d\mathbf{x}$ , its solution tends to the minimizer of this energy functional (“smoothest possible” tensor-field) for  $t \rightarrow \infty$ .

### 3 Finite element discretization schemes

To be able to apply a finite element discretization method we consider the  $n$ -tensor diffusion problem in a variational setting, where we use standard notation for Bochner spaces:

**Problem 1.** Find  $\mathbf{u} \in C^1(0, T; \mathbf{H}^1(\mathcal{M}, \mathbb{T}^n \mathcal{M}))$  such that

$$(\partial_t \mathbf{u}(t), \mathbf{v})_{\mathcal{M}} + (\nabla_{\mathcal{M}} \mathbf{u}(t), \nabla_{\mathcal{M}} \mathbf{v})_{\mathcal{M}} = 0, \quad \text{for all } \mathbf{v} \in \mathbf{H}^1(\mathcal{M}, \mathbb{T}^n \mathcal{M}), \quad (16)$$

for  $t \in (0, T]$ , subject to  $\mathbf{u}(0) = \mathbf{u}^0$ . Here  $(\cdot, \cdot)_{\mathcal{M}}$  denotes the (tensor)  $L^2$ -scalar product.

The ISFEM will be directly based on the variational formulation given in Problem 1. The other three methods, SFEM, TraceFEM, and DI, use the embedding of the surface in  $\mathbb{R}^3$  and gradient representations as presented in Section 2.2.2. For these methods applied to the  $n$ -tensor problem with  $n \geq 1$  it is natural to allow (small) *nontangential* solution components. The variational formulation given in Problem 1 is not a suitable starting point for such a finite element method, since it uses the range space  $\mathbb{T}^n \mathcal{M}$ . We now introduce, for  $n \geq 1$ , an augmented variational formulation with range space  $\mathbb{T}^n \mathbb{R}^3 \simeq \mathbb{R}^{3n}$ . It uses a term  $(\mathcal{Q}\mathbf{u}(t), \mathcal{Q}\mathbf{v})_{\mathcal{M}}$  with  $\mathcal{Q} = \text{Id} - \mathcal{P}$  the normal projection operator that is scaled by a penalty parameter  $\omega > 0$ . Note that this term vanishes for tangential functions. The augmented variational formulation reads as follows:

**Problem 2.** Assume  $n \geq 1$ . Find  $\mathbf{u} \in C^1(0, T; \mathbf{H}^1(\mathcal{M}, \mathbb{T}^n \mathbb{R}^3))$  such that

$$(\partial_t \mathcal{P}\mathbf{u}(t), \mathcal{P}\mathbf{v})_{\mathcal{M}} + (\nabla_{\mathcal{M}} \mathcal{P}\mathbf{u}(t), \nabla_{\mathcal{M}} \mathcal{P}\mathbf{v})_{\mathcal{M}} + \omega (\mathcal{Q}\mathbf{u}(t), \mathcal{Q}\mathbf{v})_{\mathcal{M}} = 0 \quad (17)$$

for all  $\mathbf{v} \in \mathbf{H}^1(\mathcal{M}, \mathbb{T}^n \mathbb{R}^3)$  and  $t \in (0, T]$ , with initial condition  $\mathbf{u}(0) = \mathbf{u}^0$ .

In (17) first derivatives appear only for the tangential components  $\mathcal{P}\mathbf{u}$ , but not for the normal components  $\mathcal{Q}\mathbf{u}$ . It is therefore natural to replace  $\mathbf{H}^1(\mathcal{M}, \mathbb{T}^n \mathbb{R}^3)$  by a larger anisotropic  $\mathbf{H}^1$  space in which only weak differentiability in tangential direction is required. To simplify the presentation we do not elaborate this.

Problem 2 is consistent with Problem 1 in the following sense. Let  $\mathbf{u}_1$  and  $\mathbf{u}_2$  be two solutions of Problem 2 and  $\mathbf{w} := \mathbf{u}_1 - \mathbf{u}_2$ . We then have  $\mathbf{w}(0) = 0$  and from (17) we obtain  $\partial_t \|\mathcal{P}\mathbf{w}\|_{\mathcal{M}}^2 \leq 0$  for  $t \in [0, T]$ . Hence  $\mathcal{P}\mathbf{w}(t) = 0$  for  $t \in [0, T]$ . Using this in (17) it follows that  $\mathcal{Q}\mathbf{w}(t) = 0$  and thus  $\mathbf{w}(t) = 0$  for  $t \in [0, T]$ . We conclude that we have uniqueness of a solution of Problem 2. It is easy to verify that a solution of Problem 1 also is a solution of Problem 2. We see that by adding the consistent penalty term, with  $\omega \geq 0$  arbitrary, we do not change the continuous solution. In general this “exact” consistency property does not hold after discretization and one then has to choose an appropriate penalty parameter value to control the consistency error, cf. Sections 3.2 and 3.3.

In SFEM and TraceFEM, introduced below, a discrete projection operator  $\mathcal{P}_h$  is used that in general is discontinuous across element boundaries. Due to this, for a vector or tensor valued finite element function  $\mathbf{u}_h$  the projected function  $\mathcal{P}_h \mathbf{u}_h$  does not have global  $H^1$ -smoothness and applying a discrete gradient to it is a delicate issue. To circumvent this, we apply the product rule to the term  $\nabla_{\mathcal{M}} \mathcal{P}\mathbf{u}$  in (17) as follows. We have  $\nabla_{\mathcal{M}} \mathcal{P}\mathbf{u} = \nabla_{\mathcal{M}} \mathbf{u} - \nabla_{\mathcal{M}} \mathcal{Q}\mathbf{u}$ . For a vector field  $\mathbf{u} = \mathbf{u}^{(1)}$  one easily checks that  $\nabla_{\mathcal{M}} \mathcal{Q}\mathbf{u} = \nabla_{\mathcal{M}}((\mathbf{n} \otimes \mathbf{n})\mathbf{u}) = -\langle \mathbf{u}, \mathbf{n} \rangle \mathbf{H}$  holds. Hence, we obtain  $\nabla_{\mathcal{M}} \mathcal{P}\mathbf{u} = \nabla_{\mathcal{M}} \mathbf{u} + \langle \mathbf{u}, \mathbf{n} \rangle \mathbf{H}$  and the representation on the right-hand side is suitable for a finite element approximation. We introduce the notation  $G(\mathbf{u}) := \langle \mathbf{u}, \mathbf{n} \rangle \mathbf{H}$ . Note that  $G$



depends on the extended Weingarten map. Similar results hold for  $n \geq 2$ . In tensor notation we obtain the following identities:

$$\begin{aligned} [\nabla_{\mathcal{M}} \mathcal{Q}\mathbf{u}^{(1)}]^{i_1 i_2} &= [G(\mathbf{u})]^{i_1 i_2} := -H^{i_1 i_2} u^k n_k, & n = 1, \\ [\nabla_{\mathcal{M}} \mathcal{Q}\mathbf{u}^{(2)}]^{i_1 i_2 i_3} &= [G(\mathbf{u})]^{i_1 i_2 i_3} := -H^{i_1 i_3} P_j^{i_2} u^{kj} n_k - H^{i_2 i_3} P_j^{i_1} u^{jk} n_k, & n = 2. \end{aligned} \quad (18)$$

Thus we have the following alternative representation of the second term in (17), which will be the one used in SFEM and TraceFEM below:

$$(\nabla_{\mathcal{M}} \mathcal{P}\mathbf{u}(t), \nabla_{\mathcal{M}} \mathcal{P}\mathbf{v})_{\mathcal{M}} = (\nabla_{\mathcal{M}} \mathbf{u}(t) + G(\mathbf{u}(t)), \nabla_{\mathcal{M}} \mathbf{v} + G(\mathbf{v}))_{\mathcal{M}}. \quad (19)$$

In the following subsections we briefly treat four known finite element discretization methods and apply these methods for spatial discretization of the  $n$ -tensor heat problem. We combine these spatial discretizations with a standard BDF-2 time discretization. We start with ISFEM, which is the “most conforming” method in the sense that it is based on the variational formulation in Problem 1. This method uses intrinsic gradient representations. The methods SFEM, TraceFEM, and DI are based on the formulation in Problem 2 and make use of gradient representations in the embedding space. In the DI method an additional approximation of the inner products is considered by “extending” the PDE in a domain  $\Omega \subset \mathbb{R}^3$  that contains the surface  $\mathcal{M}$  and numerically restricting the integrals to  $\mathcal{M}$  using a smeared-out Dirac-delta function. This method is not consistent in the sense that the solution of the extended PDE, restricted to  $\mathcal{M}$ , does *not* coincide with the solution of the Problems 1 and 2. In this sense, the DI approach is the “least conforming” one. In the presentation of the methods we restrict to the lowest order finite element case. In remarks we will briefly comment on extensions to higher order finite elements.

In Section 3.5 we discuss and compare the four methods and in particular address the issues a)–c) formulated in the Introduction.

### 3.1 Intrinsic Surface Finite Element Method (ISFEM)

The ISFEM has so far only been introduced for scalar-valued problems in [1]. We briefly review the scalar ISFEM setting and extend it to the case of a vector-valued problem. Analogously, an extension to tensor fields is possible, but it has not yet been addressed. The main idea of ISFEM is to consider the formulation as given in Problem 1 and discretize it in local coordinates with the intrinsic differential operators containing all the geometric information. We will consider the local coordinates  $\hat{\mathbf{s}} = (\hat{s}^1, \hat{s}^2)$  with respect to the orthogonal tangent vectors  $\tilde{\mathbf{t}}_1, \tilde{\mathbf{t}}_2$ , and the intrinsic differential operators defined employing eq. (5).

Let  $\mathcal{S}_{\mathcal{M}}$  be a (curved) exact surface triangulation, formed by a set of non-intersecting (curved) surface triangles with vertices on  $\mathcal{M}$ , such that  $\mathcal{M} = \bigcup \{S \in \mathcal{S}_{\mathcal{M}}\}$ . We will introduce *conforming* subspaces  $\mathbf{V}_{\mathcal{M}}^{(n)}$  such that the relation  $\mathbf{H}^1(\mathcal{M}, \mathbf{V}_{\mathcal{M}}^{(n)}) \subset \mathbf{H}^1(\mathcal{M}, \mathbb{T}^n \mathcal{M})$  holds, cf. Problem 1. These spaces are used in an approximate Galerkin discretization of Problem 1, in the sense that the surface integrals  $(\cdot, \cdot)_{\mathcal{S}}$  are approximated using a quadrature rule.

We denote by  $(\mathbf{u}, \mathbf{v})_h := \sum_q w_q \langle \mathbf{u}(\mathbf{x}_q), \mathbf{v}(\mathbf{x}_q) \rangle_{\tilde{\mathbf{g}}(\mathbf{x}_q)} \sqrt{|\tilde{\mathbf{g}}(\mathbf{x}_q)|}$  such an approximation of the surface integrals  $(\mathbf{u}, \mathbf{v})_S$  by a quadrature rule with  $\mathbf{x}_q \in S$  the quadrature points and  $w_q \in \mathbb{R}$  the associated quadrature weights. Concerning practical computation, the key point is the need of geometric information only at quadrature points, in an exact or approximated way.

**Remark 1.** *In the considered benchmark problem, see Section 4, we consider a Gauss quadrature rule of order three. In this case, we make use of the knowledge of the parametrization of the surface to assign geometric information at the quadrature points.*

We first consider the scalar case  $n = 0$ . The function space  $\mathbf{V}_{\mathcal{M}}^{(0)} = \text{span}(\{\psi_l\})$  is spanned by continuous basis functions  $\psi_l: \mathcal{M} \rightarrow \mathbb{R}$  that are obtained by formally gluing together localized functions  $\psi_l^S: S \rightarrow \mathbb{R}$  for  $S \in \mathcal{S}_{\mathcal{M}}$ . For each element  $S \in \mathcal{S}_{\mathcal{M}}$ , we consider the associated element  $\hat{S} = \boldsymbol{\mu}^{-1}(S)$  in the reference domain and we define the classical linear Lagrange nodal basis functions  $\hat{\psi}_l^{\hat{S}}(\hat{\mathbf{x}})$  in reference local coordinates  $\hat{\mathbf{x}} \in \hat{S}$ . Denoting by  $\mathbf{x} = \boldsymbol{\mu}(\hat{\mathbf{x}}) \in S$  the corresponding associated surface coordinates in  $S$ , then the surface basis functions are simply lifted via this mapping, i.e.,  $\psi_l^S(\mathbf{x}) := \hat{\psi}_l^{\hat{S}}(\hat{\mathbf{x}})$ . In order to compute gradients in the tangential basis representation  $\{\tilde{\mathbf{t}}_1, \tilde{\mathbf{t}}_2\}$  associated to coordinates  $\hat{\mathbf{s}}$ , instead of the natural tangential basis  $\{\mathbf{t}_1, \mathbf{t}_2\}$  associated to  $\hat{\mathbf{x}}$ , we need to perform a coordinate transformation, i.e.,

$$\nabla_{\mathcal{M}} \psi_l^S(\mathbf{x}) := \tilde{\mathbf{g}}^{-1} \mathbf{W} \hat{\nabla} \hat{\psi}_l^{\hat{S}}(\hat{\mathbf{x}}),$$

where  $\mathbf{W} = \tilde{\mathbf{J}}^+ \mathbf{J}$  is the Jacobian of the change of coordinates between  $\hat{\mathbf{x}}$  and  $\hat{\mathbf{s}}$ , with  $\tilde{\mathbf{J}} = [\tilde{\mathbf{t}}_1, \tilde{\mathbf{t}}_2]$  and  $\mathbf{J} = [\mathbf{t}_1, \mathbf{t}_2]$ .

**Remark 2.** *In the case of a surface obtained by the graph of a scalar function, e.g.,  $\boldsymbol{\mu}(\hat{\mathbf{x}}) = (\hat{x}^1, \hat{x}^2, f(\hat{x}^1, \hat{x}^2))^T = \mathbf{x} \in \mathcal{M}$ , the matrix  $\mathbf{W}$  is directly obtained from the  $2 \times 2$  block of  $\tilde{\mathbf{J}}^T$  corresponding to the independent variables.*

The discrete scalar functions  $\mathbf{u}_h^{(0)} \in \mathbf{V}_{\mathcal{M}}^{(0)}$  can be expanded in terms of the basis functions as  $\mathbf{u}_h^{(0)}(\mathbf{x}) = \sum_l u_l \psi_l(\mathbf{x})$ , with  $u_l$  the scalar coefficient associated to the basis function  $\psi_l$ . For discrete vector-valued functions  $\mathbf{u}_h^{(1)}$  we exploit the orthogonal covariant reference frame  $\{\tilde{\mathbf{t}}_1, \tilde{\mathbf{t}}_2\}$  and represent the solution in contravariant components, i.e.,  $\underline{\mathbf{u}}^{(1)} = [u^i]$ , for  $i = 1, 2$ . Each component  $u^i$  can be approximated by the discrete functions  $u_h^i = \sum_l u_l^i \psi_l$ , with  $\{\psi_l\}_l$  the set of scalar basis functions of  $\mathbf{V}_{\mathcal{M}}^{(0)}$ . Thus we get

$$\mathbf{u}_h^{(1)}(t) = \sum_l u_l^1(t) \psi_l \tilde{\mathbf{t}}_1 + u_l^2(t) \psi_l \tilde{\mathbf{t}}_2,$$

which gives rise to the definition of a discrete vector function space:

$$\mathbf{V}_{\mathcal{M}}^{(1)} := \{ \mathbf{v}_h = v_h^1 \tilde{\mathbf{t}}_1 + v_h^2 \tilde{\mathbf{t}}_2 \mid v_h^1, v_h^2 \in \mathbf{V}_{\mathcal{M}}^{(0)} \}.$$

The same idea can be applied to define a discrete tensor function space  $\mathbf{V}_{\mathcal{M}}^{(n)}$ .

By applying the definition of gradients and scalar product in section 2.2.1, with respect to the orthogonal reference frame  $\{\tilde{\mathbf{t}}_1, \tilde{\mathbf{t}}_2\}$ , and the quadrature rule  $(\cdot, \cdot)_h$ , we obtain the semi-discrete ISFEM discretization of Problem 1:

**Problem 3.** Find  $\mathbf{u}_h(t) = \mathbf{u}_h^{(n)}(t) \in \mathbf{V}_{\mathcal{M}}^{(n)}$  such that

$$(\partial_t \mathbf{u}_h(t), \mathbf{v}_h)_h + (\nabla_{\mathcal{M}} \mathbf{u}_h(t), \nabla_{\mathcal{M}} \mathbf{v}_h)_h = 0, \quad \text{for all } \mathbf{v}_h \in \mathbf{V}_{\mathcal{M}}^{(n)} \quad (20)$$

for  $t \in (0, T]$ , with initial condition  $\mathbf{u}_h(0) = \mathbf{u}^0$ .

We obtain fully discrete schemes by applying a BDF-2 discretization scheme to the semi-discrete problem (20).

### 3.2 Surface Finite Element Method (SFEM)

The essence of the lowest order SFEM is the approximation of  $\mathcal{M}$  by a (shape regular) triangulation, consisting of flat triangles, and the use of globally continuous piecewise linears on this triangulation for approximation of the continuous solution. This technique avoids surface parametrizations and (for scalar problems) is very similar to a standard finite element method in a flat domain. The piecewise triangular surface approximation is denoted by  $\mathcal{M}_h$ . The space of globally continuous piecewise linears on  $\mathcal{M}_h$  is denoted by  $V_{\mathcal{M}_h}$ . We introduce the natural geometry normals  $\mathbf{n}_h|_S$ , with  $S$  a triangle from  $\mathcal{M}_h$ , that are formally glued together to build the discrete surface normal field  $\mathbf{n}_h$ . The discrete tangential projection is given by  $\mathbf{P}_h = \mathbf{I} - \mathbf{n}_h \otimes \mathbf{n}_h$ . The SFEM for the scalar case is well-known in the literature and reads as follows (cf. Problem 2), with  $\nabla_{\mathcal{M}_h} \mathbf{v}_h = \mathbf{P}_h \nabla \bar{\mathbf{v}}_h$  the discrete analogon of the surface gradient as in (9):

**Problem 4** (Scalar problem). Find  $\mathbf{u}_h = \mathbf{u}_h^{(0)} \in C^1(0, T; V_{\mathcal{M}_h})$  such that

$$(\partial_t \mathbf{u}_h(t), \mathbf{v}_h)_{\mathcal{M}_h} + (\nabla_{\mathcal{M}_h} \mathbf{u}_h(t), \nabla_{\mathcal{M}_h} \mathbf{v}_h)_{\mathcal{M}_h} = 0, \quad \text{for all } \mathbf{v}_h \in V_{\mathcal{M}_h} \quad (21)$$

and for all  $t \in (0, T]$  subject to an initial condition  $\mathbf{u}_h(0) = \mathbf{I}_h \mathbf{u}^0$ . Here  $\mathbf{I}_h$  denotes the nodal interpolation operator in the finite element space  $V_{\mathcal{M}_h}$ .

Using the nodal finite element basis in the space  $V_{\mathcal{M}_h}$  results in a ODE system for the coefficients of  $\mathbf{u}_h$ .

We now consider  $n \geq 1$ . The discretization is based on the formulation in Problem 2, combined with a componentwise approximation using SFEM for scalar-valued problems. For a detailed description for tensor-valued problems see [21, 13, 14].

The discrete tensor projection operator  $\mathcal{P}_h$  is defined in analogy to eq. (8). A corresponding orthogonal projection  $\mathcal{Q}_h = \mathcal{I} - \mathcal{P}_h$  naturally follows. We use the surface finite element space  $\mathbf{V}_{\mathcal{M}_h}^{(n)} = [V_{\mathcal{M}_h}]^N$  as the product space of  $N = 3^n$  scalar Lagrange spaces. A discrete surface gradient  $\nabla_{\mathcal{M}_h}$  is defined as in (10)–(11), but with the continuous projections replaced by the discrete analogons. Error analysis and numerical experiments show that replacing the projection operator  $\mathcal{Q}$  in the penalty term of the continuous variational formulation by its discrete analogon  $\mathcal{Q}_h$  is *not* satisfactory, since

it results in suboptimal convergence in the  $L^2$ -norm, cf. [13]. Optimal convergence is obtained if one instead uses a projection operator based on a normal  $\mathbf{n}_h^+$  that is a *one order more accurate approximation* of  $\mathbf{n}$  than the  $\mathcal{M}_h$ -normal  $\mathbf{n}_h$ . We denote such a modified (“higher order”) projection by  $\mathcal{Q}_h^+$ .

Thus we obtain the following SFEM discretization of eq. (17), where we use the result (19), see also [14]:

**Problem 5.** Take  $n \geq 1$ . Find  $\mathbf{u}_h = \mathbf{u}_h^{(n)} \in C^1(0, T; \mathbf{V}_{\mathcal{M}_h}^{(n)})$  such that

$$\begin{aligned} (\partial_t \mathcal{P}_h \mathbf{u}_h(t), \mathcal{P}_h \mathbf{v}_h)_{\mathcal{M}_h} + (\nabla_{\mathcal{M}_h} \mathbf{u}_h(t) + G_h(\mathbf{u}_h(t)), \nabla_{\mathcal{M}_h} \mathbf{v}_h + G_h(\mathbf{v}_h))_{\mathcal{M}_h} \\ + \beta h^{-2} (\mathcal{Q}_h^+ \mathbf{u}_h(t), \mathcal{Q}_h^+ \mathbf{v}_h)_{\mathcal{M}_h} = 0 \quad \text{for all } \mathbf{v}_h \in \mathbf{V}_{\mathcal{M}_h}^{(n)} \end{aligned} \quad (22)$$

and for all  $t \in (0, T]$  subject to an initial condition  $\mathbf{u}_h(0) = \mathbf{I}_h \mathbf{u}^0$ .

Here  $G_h(\cdot)$  is a discrete analogon of  $G(\cdot)$  in (19), e.g., for  $n = 1$ ,  $G_h(\mathbf{v}_h) = \langle \mathbf{v}_h, \mathbf{n}_h \rangle \mathbf{H}_h$ , where  $\mathbf{H}_h$  is an approximation of the Weingarten mapping. The parameter  $\beta > 0$  is a penalty parameter. The scaling with  $h^{-2}$  in the penalty term follows from an error analysis, cf. [13, 14].

**Remark 3.** The discrete Weingarten map  $\mathbf{H}_h$  can be computed from the gradient of the elementwise gradient of the discrete normal field  $\mathbf{n}_h$ . Utilizing the representation  $\mathbf{n}_h = \mathbf{m}_h / \|\mathbf{m}_h\|$  with  $\mathbf{m}_h$  the cross-product of the columns of  $\mathbf{J}_h$  and thus a discrete function, we can compute,  $\mathbf{H}_h = \mathcal{P}_h \nabla \mathbf{n}_h = \|\mathbf{m}_h\|^{-1} \mathcal{P}_h \nabla (\mathbf{I}_h \mathbf{m}_h)$ .

**Remark 4.** In case the surface  $\mathcal{M}$  is described by the coordinate mapping  $\boldsymbol{\mu}$ , higher order surface approximations than piecewise linear can be obtained by (Lagrange) interpolation  $\boldsymbol{\mu}_h = \mathbf{I}_h \boldsymbol{\mu}$ . With discrete functions defined in the reference domain and lifted to the discrete surface using  $\boldsymbol{\mu}_h$ , a higher-order function space  $V_{\mathcal{M}}$  can be constructed, cf. [8]. Similar to the piecewise flat surface and linear function setting, geometric quantities are obtained by derivatives of the discrete parametrization  $\boldsymbol{\mu}_h$ . This allows to obtain also high-order convergence for the projection based scheme, cf. [13, 14].

If derivatives of the continuous parametrization  $\boldsymbol{\mu}$  are directly available and computable, also an exact parametrization of the surface geometry, cf. Section 3.1, is possible and is used in the numerical example to compute a reference solution.

The discretization in time follows standard approaches and is therefore not described in detail. We consider a classical BDF-2 scheme.

### 3.3 Trace Finite Element Method (TraceFEM)

The TraceFEM is based on the same variational Problem 2 as the SFEM. The former uses a finite element space which is defined on a background volumetric mesh that is not fitted to the surface. The geometry approximation is based on an implicit description of the surface using a level set approach. For an overview of TraceFEM we refer to [22].

We assume the surface  $\mathcal{M}$  to be represented as the zero level of a level set function  $\phi$ . We denote by  $\Omega$  a sufficiently small polygonal 3d neighborhood of the surface. The

surface approximation is based on a piecewise linear approximation  $\phi_h$  (e.g., linear interpolation) of  $\phi$  and given by  $\mathcal{M}_h := \{\mathbf{x} \in \Omega \mid \phi_h(\mathbf{x}) = 0\}$ . Let  $\mathcal{S}_\Omega$  be a shape regular tetrahedral triangulation of  $\Omega$  and  $V_\Omega$  the standard finite element spaces of continuous piecewise linear polynomials on  $\mathcal{S}_\Omega$ . For higher order constructions of  $\mathcal{M}_h$  we refer to Remark 5. We introduce the set  $\mathcal{S}_\Omega^{\mathcal{M}_h}$ , consisting of all tetrahedra  $S \in \mathcal{S}_\Omega$  that have a nonzero intersection with  $\mathcal{M}_h$ . The domain formed by all these tetrahedra is denoted by  $\Omega^{\mathcal{M}_h} = \bigcup \{S \in \mathcal{S}_\Omega^{\mathcal{M}_h}\}$ . On  $\Omega^{\mathcal{M}_h}$ , we define by simple restriction the scalar finite element space  $V_\Omega^{\mathcal{M}_h} := \{v|_{\Omega^{\mathcal{M}_h}} \mid v \in V_\Omega\}$ . A corresponding  $n$ -tensor finite element space is given by  $\mathbf{V}_\Omega^{\mathcal{M}_h} := [V_\Omega^{\mathcal{M}_h}]^N$  with  $N = 3^n$ . To avoid instabilities due to small cuts of  $\mathcal{M}_h$  in the triangulation  $\Omega^{\mathcal{M}_h}$  one uses a so-called normal derivative volume stabilization [5, 11]. Again  $\mathbf{n}_h$  denotes the piecewise normal field on  $\mathcal{M}_h$ ,  $\mathbf{P}_h = \mathbf{I} - \mathbf{n}_h \otimes \mathbf{n}_h$  and the discrete tensor projection operator  $\mathcal{P}_h$  is defined as in Subsection 3.2.

We now describe the method for the scalar case  $n = 0$ . The stabilization is then given by  $s_h(\mathbf{u}_h, \mathbf{v}_h) := (\mathbf{n}_h \cdot \nabla \mathbf{u}_h, \mathbf{n}_h \cdot \nabla \mathbf{v}_h)_{\Omega^{\mathcal{M}_h}}$ . The discrete problem is as follows, cf. Problem 4:

**Problem 6** (Scalar problem). *Find  $\mathbf{u}_h = \mathbf{u}_h^{(0)} \in C^1(0, T; V_\Omega^{\mathcal{M}_h})$  such that*

$$(\partial_t \mathbf{u}_h(t), \mathbf{v}_h)_{\mathcal{M}_h} + (\nabla_{\mathcal{M}_h} \mathbf{u}_h(t), \nabla_{\mathcal{M}_h} \mathbf{v}_h)_{\mathcal{M}_h} + \beta' h^{-1} s_h(\mathbf{u}_h(t), \mathbf{v}_h) = 0 \quad (23)$$

for all  $\mathbf{v}_h \in V_\Omega^{\mathcal{M}_h}$  and all  $t \in (0, T]$ , subject to an initial condition  $\mathbf{u}_h(0) = \mathbf{I}_\Omega^{\mathcal{M}_h} \bar{\mathbf{u}}^0$ . Here  $\mathbf{I}_\Omega^{\mathcal{M}_h}$  denotes the nodal interpolation operator in the finite element space  $V_\Omega^{\mathcal{M}_h}$ .

Note that compared to Problem 4 we use a different finite element space and added the stabilization term  $s_h(\cdot, \cdot)$ .

We now consider  $n \geq 1$ . In the same spirit as in the SFEM, cf. Problem 5, it is based on the variational formulation in Problem 2. The normal derivative volume stabilization takes the form

$$s_h(\mathbf{u}, \mathbf{v}) := \int_{\Omega^{\mathcal{M}_h}} (\nabla \mathbf{u}_{n+1} \mathbf{n}_h) \cdot (\nabla \mathbf{v}_{n+1} \mathbf{n}_h) \, dx,$$

and we obtain the following discretization of (17):

**Problem 7.** *Take  $n \geq 1$ . Find  $\mathbf{u}_h = \mathbf{u}_h^{(n)} \in C^1(0, T; \mathbf{V}_\Omega^{\mathcal{M}_h})$  such that*

$$\begin{aligned} & (\partial_t \mathcal{P}_h \mathbf{u}_h(t), \mathcal{P}_h \mathbf{v}_h)_{\mathcal{M}_h} + (\nabla_{\mathcal{M}_h} \mathbf{u}_h(t) + G_h(\mathbf{u}_h(t)), \nabla_{\mathcal{M}_h} \mathbf{v}_h + G_h(\mathbf{v}_h))_{\mathcal{M}_h} \\ & + \beta h^{-2} (\mathcal{Q}_h^+ \mathbf{u}_h(t), \mathcal{Q}_h^+ \mathbf{v}_h)_{\mathcal{M}_h} + \beta' h^{-1} s_h(\mathbf{u}_h(t), \mathbf{v}_h) = 0 \quad \text{for all } \mathbf{v}_h \in \mathbf{V}_\Omega^{\mathcal{M}_h} \end{aligned} \quad (24)$$

and for all  $t \in (0, T]$  subject to an initial condition  $\mathbf{u}_h(0) = \mathbf{I}_\Omega^{\mathcal{M}_h} \bar{\mathbf{u}}^0$ , with  $\beta > 0$  a penalty parameter and  $\beta' > 0$  a stabilization parameter.

As in Section 3.2 we use an ‘‘improved’’ projection  $\mathcal{Q}_h^+$  based on a higher order normal approximation. A motivation for this improved projection and a construction of an improved normal approximation are given in [15]. As in SFEM the term  $G_h(\cdot)$  is a discrete analogon of  $G(\cdot)$  given in (19). The semi-discrete Problem 7 is essentially the same as the SFEM Problem 5, except for the additional stabilization term  $s_h(\cdot, \cdot)$ .

As in Section 3.2, we use a classical BDF-2 scheme for time discretization.

**Remark 5.** To obtain a higher order discretization method an isoparametric mapping  $\Theta_h$  is the key ingredient. The main idea and construction of this mapping is explained in [17]. It is based on a level set function approximation  $\phi_h \in V_\Omega^k$  of order  $k$ . This function implicitly defines a surface approximation. For  $k \geq 2$  numerical integration is hard to realize. To obtain a computationally efficient method a piecewise triangular surface approximation  $\mathcal{M}^{lin}$  is used, defined as follows. Let  $\hat{\phi}_h = I^1 \phi_h$  be the linear nodal interpolation of the higher order level set function approximation  $\phi_h$ . Based on this we define

$$\mathcal{M}_h := \Theta_h(\mathcal{M}^{lin}) = \{\mathbf{x} \mid \hat{\phi}_h(\Theta_h^{-1}(\mathbf{x})) = 0\}.$$

In the same manner, the parametric mapping induces (higher order) finite element spaces.

### 3.4 Diffuse-Interface Approach (DI)

The DI method, see [23, 18, 20], considers an approximation of eq. (17), which is a classical problem in the embedding space  $\mathbb{R}^3$  and thus leads to a set up where established standard volume FEM can be applied. Similar to Section 3.3 the geometry approximation is based on an implicit description of the surface, but instead of a level set approach a phase field description is used. We define

$$\phi_\epsilon(\mathbf{x}) := \frac{1}{2} \left( 1 - \tanh \left( \frac{3}{\epsilon} \rho(\mathbf{x}) \right) \right), \quad \delta_\epsilon(\mathbf{x}) := \frac{36}{\epsilon} \phi_\epsilon^2(\mathbf{x}) (1 - \phi_\epsilon(\mathbf{x}))^2,$$

for  $\mathbf{x} \in U_\delta(\mathcal{M})$  with  $0 < \epsilon < \delta$  an interface thickness parameter. The phase-field function  $\varphi_\epsilon$  is based on the signed-distance representation  $\rho$  of  $\mathcal{M}$ . With this definition of  $\varphi_\epsilon$  we obtain  $\delta_\epsilon \rightarrow \delta_{\mathcal{M}}$  for  $\epsilon \rightarrow 0$ , with  $\delta_{\mathcal{M}}$  the surface delta-function to  $\mathcal{M}$ . We define an extension of scalar-valued fields defined on  $\mathcal{M}$  to the neighborhood  $U_\delta(\mathcal{M})$  by using the closest point projection,  $\bar{f}(\mathbf{x}) := f(\pi(\mathbf{x})) = f(\mathbf{x} - \rho(\mathbf{x})\nabla\rho(\mathbf{x}))$  for  $\mathbf{x} \in U_\delta(\mathcal{M})$ . Into the rest of the domain  $\Omega$ , the function  $f$  is extended in an approximate way, e.g., using fast-marching algorithms, or a Hopf–Lax algorithm [6]. The scalar-valued phase-field function  $\varphi_\epsilon$  and delta-function  $\delta_\epsilon$  are extended with a constant value. Vector and tensor fields are extended by a componentwise extension of the embedded description.

As in Section 3.3 let  $\mathcal{S}_\Omega$  be a shape regular tetrahedral triangulations of  $\Omega$  and  $V_\Omega$  be the standard finite element spaces of continuous piecewise linears defined on  $\mathcal{S}_\Omega$ . We define the tensor finite element space  $\mathbf{V}_\Omega^{(n)} := [V_\Omega]^N$  as the product of  $N = 3^n$  scalar finite element spaces.

For scalar fields  $\mathbf{u}^{(0)}$  the FEM discretization of the DI approximation of eq. (16) reads

**Problem 8** (Scalar diffuse interface approach [23]). Find  $\mathbf{u}_h = \mathbf{u}_h^{(0)} \in C^1(0, T; V_\Omega)$  such that

$$\sum_{S \in \mathcal{S}_\Omega} (\delta_\epsilon \partial_t \mathbf{u}_h(t), \mathbf{v}_h)_S + \left( \hat{\delta}_\epsilon \nabla \mathbf{u}_h(t), \nabla \mathbf{v}_h \right)_S = 0 \quad (25)$$

for all  $\mathbf{v}_h \in V_\Omega$  and for all  $t \in (0, T]$ , subject to the initial condition  $\mathbf{u}_h(0) = \bar{\mathbf{u}}^0$ . We denote by  $\hat{\delta}_\epsilon = \max\{\delta_\epsilon, \sigma\}$  the regularized surface delta-function approximation, with  $\sigma = 10^{-8}$  in the numerical examples.

For vector fields  $\mathbf{u}^{(1)}$  we consider the componentwise reformulation of the surface problem as in eq. (17). For such a formulation we apply the scalar DI approach for each component. This requires geometric properties of the surface, namely the normal  $\mathbf{n}$  and curvature  $\mathbf{H}$  in the  $\epsilon$ -neighborhood of  $\mathcal{M}$ . To obtain these quantities one can use a numerical approximation of the signed-distance function  $\rho^\epsilon$  in  $\Omega$  and define  $\mathbf{n}^\epsilon := \nabla \rho^\epsilon$  and  $\mathbf{H}^\epsilon := -\nabla^2 \rho^\epsilon$ , as well as the associated projections by  $\mathbf{P}^\epsilon$ ,  $\mathcal{P}^\epsilon$ , and  $\mathcal{Q}^\epsilon$  in terms of  $\mathbf{n}^\epsilon$ .

**Problem 9.** Assume  $n \geq 1$ . Find  $\mathbf{u}_h \in C^1(0, T; \mathbf{V}_\Omega^{(n)})$  such that

$$\begin{aligned} \sum_{S \in \mathcal{S}_\Omega} (\delta_\epsilon \partial_t \mathcal{P}^\epsilon \mathbf{u}_h(t), \mathcal{P}^\epsilon \mathbf{v}_h)_S + (\delta_\epsilon \nabla_S \mathcal{P}^\epsilon \mathbf{u}_h(t), \nabla_S \mathcal{P}^\epsilon \mathbf{v}_h)_S + \beta (\delta_\epsilon \mathcal{Q}^\epsilon \mathbf{u}_h(t), \mathcal{Q}^\epsilon \mathbf{v}_h)_S \\ + \sum_{S \in \mathcal{S}_\Omega} \sigma ((1 - C_\epsilon \delta_\epsilon) \nabla \mathbf{u}_h(t), \nabla \mathbf{v}_h)_S = 0 \end{aligned} \quad (26)$$

for all  $\mathbf{v}_h \in \mathbf{V}_\Omega^{(n)}$  and for all  $t \in (0, T]$  subject to the initial condition  $\mathbf{u}_h(0) = \bar{\mathbf{u}}^0$ , with  $\beta > 0$  a penalization factor and  $C_\epsilon = 1/\max(\delta_\epsilon) = 4/9\epsilon$ .

The additional term in the second line provides a regularization for numerical conditioning of the resulting linear system. In the spirit of the scalar case, we add a small amount of ‘‘additional diffusion’’ to the domain off the interface. This domain is described by  $(1 - C_\epsilon \delta_\epsilon)$ .

Similar to section 3.3 the discrete covariant derivative  $\nabla_S$  is described along a componentwise description and extended to the embedding space by using the extended geometric quantities  $\mathbf{n}^\epsilon$ ,  $\mathbf{P}^\epsilon$ , and  $\mathbf{H}^\epsilon$ , cf. (18).

**Remark 6.** In the considered benchmark problem, see Section 4, we use an embedding domain  $\Omega = [-2, 2]^3$  which is discretized by a hierarchical tetrahedra mesh. To be computational efficient and to ensure an appropriate resolution of  $\delta_\epsilon$  an adaptive refinement with about 7–11 grid points across the interface,  $\varphi_\epsilon \in [0.05, 0.95]$ , should be used while a very coarse grid in the remaining part of  $\Omega$  is sufficient. For  $\mathcal{S}_\Omega$  we define the grid size  $h$  by the shortest edge length of the smallest elements, typically located at the interface. To approximate the benchmark surface we refine the mesh according the interface thickness of  $\epsilon = 0.125$ , resulting in a grid size of  $h = 0.0156$ . On this grid we use the `meshconv` tool [26] to obtain the approximate distance function  $\rho_\epsilon$ . To obtain a numerical approximation with sufficient quality of normals and curvatures as derivatives of  $\rho$  requires a proper resolution of the considered surface. Such resolution implies  $\epsilon < \delta$  with  $\delta$  the smallest curvature radius of the considered surface. In the benchmark this implies a very small  $\epsilon$  yielding non feasible numerical effort. Therefore we use the analytic descriptions of  $\mathbf{n}$  and  $\mathbf{H}$  evaluate and extend them component wise on  $\mathcal{S}_\Omega$  using the Hopf-Lax algorithm. We further consider  $\beta = 1000$ .

### 3.5 Discussion of the methods

We discuss several issues that are important for the numerical treatment of  $n$ -tensor surface PDEs, in particular the issues listed in the Introduction.

First note that there is the following key difference between ISFEM, SFEM, TraceFEM and DI. The first three methods are directly based on the (variational) PDEs in Problems 1 and 2, which are *consistent*, in the sense that these have the same solution which also coincides with the solution of the  $n$ -tensor heat equation in strong formulation. The DI approach on the other hand is based on an  $\epsilon$ -dependent PDE (in a small volumetric neighborhood of the surface), the solution of which, restricted to the surface, in general differs from that of the Problems 1, 2. The formulation only formally converges to the  $n$ -tensor heat equation as  $\epsilon \rightarrow 0$ .

*Surface representation.* The representation of the surface  $\mathcal{M}$  is either explicit, in ISFEM and SFEM, or implicit, in TraceFEM and DI. The explicit approach in ISFEM is based on the existence of a parametrization of the surface by an atlas. In SFEM one only needs an approximate surface triangulation. In ISFEM quadrature one needs (exact or approximated) geometric information from the local chart at the quadrature points. In SFEM the quadrature is very simple because only integrals over flat triangles have to be computed. The implicit description of the surface in TraceFEM and DI is based on a level set description  $\phi$  or a phase field description  $\phi_\epsilon$  of  $\mathcal{M}$ , respectively. In TraceFEM, based on a piecewise linear approximation of  $\phi$ , a surface approximation  $\mathcal{M}_h$  consisting of triangles is constructed. This requires techniques for computing cuts of tetrahedra with zero levels of linear functions. Due to the fact that the resulting triangulation is in general not shape regular (“small cuts”) one needs a stabilization (the normal volume derivative stabilization term). As in SFEM quadrature is very simple because only integrals over triangles (and tetrahedra) have to be computed. Whereas in TraceFEM an explicit reconstruction  $\mathcal{M}_h$  of the implicit surface is determined, the surface remains implicit in the DI method. In the discrete variational problems of DI only integrals over tetrahedra are involved. Hence, quadrature is straightforward. Information of the surface enters (only) via the signed-distance function  $\rho$  that is needed in the phase-field function  $\phi_\epsilon$ . This distance computation requires an additional preprocessing step.

*Representation of the gradient operator and geometry information.* On surfaces there are different natural representations of differential operators, e.g. gradient and divergence. In ISFEM the intrinsic representation of the gradient based on local coordinates is used. One then needs a basis of the tangent spaces (at discrete points on the surface). In ISFEM the orthogonal basis  $\{\tilde{\mathbf{t}}_1, \tilde{\mathbf{t}}_2\}$  is employed. The other three methods SFEM, TraceFEM, and DI use a representation of the surface gradient based on the standard gradient in  $\mathbb{R}^3$ .

We now briefly discuss important differences concerning geometric information between  $n = 0$  and  $n \geq 1$ . In the ISFEM, for  $n = 0$  one needs the metric tensor (at discrete points on the surface) and for  $n \geq 1$  one in addition needs information about derivatives of the metric coefficients. For SFEM and TraceFEM in the case  $n = 0$  one needs (only) the discrete normal  $\mathbf{n}_h$ , whereas for  $n \geq 1$  a more accurate normal approximation (used in  $\mathcal{Q}_h^+$ ) and an approximation  $\mathbf{H}_h$  of the Weingarten mapping (used in  $G_h(\cdot)$ ) are needed. In the DI method, for  $n = 0$  we need (approximate) evaluations of the signed distance functions  $\rho$  and for  $n \geq 1$  we in addition need (approximate) evaluations of  $\nabla\rho$ .

For  $n \geq 1$ , due to the different representations used, there is the following difference



between ISFEM and the other three methods. The methods, SFEM, TraceFEM, and DI, represent the  $n$ -tensor fields in the embedding space as element of  $\mathbb{R}^{3^n}$ . For  $n \geq 1$  the number of tensor components in the embedding space is larger than in the intrinsic representation used in ISFEM and this discrepancy grows with increasing tensorial rank  $n$ .

*Tangentiality condition.* A further significant difference between  $n = 0$  and  $n \geq 1$  comes from the tangentiality condition, which is nontrivial only for  $n \geq 1$ . In ISFEM this condition is automatically satisfied due to the intrinsic representation used. In SFEM and TraceFEM it is treated by discretization of the augmented variational formulation in Problem 2, which involves the consistent penalty term with the projection  $\mathcal{Q}$ . Thus, an additional term in the variational form is introduced and in the discrete setting an appropriate scaling of this term is essential. In DI a volumetric variant  $\mathcal{Q}^\epsilon$  of  $\mathcal{Q}$  is introduced to satisfy the tangentiality condition approximately. Note that on the continuous level, in Problem 2, due to the additional penalty term the tangentiality condition is satisfied exactly whereas this is not the case for the continuous formulation used in the DI method.

Finally we briefly comment on parameters used in the different methods. In all four methods we have the mesh size parameter  $h$ , which in ISFEM and SFEM refers to a (approximate) surface triangulation whereas in TraceFEM and DI this  $h$  corresponds to the mesh size of a tetrahedral triangulation of a volumetric domain that contains the surface. In all four methods we have a time step discretization parameter  $\Delta t$ . In all four methods one can choose the degree  $k$  of the finite elements used. In the presentation above we restricted to  $k = 1$ . In ISFEM we have no further parameters. In SFEM and TraceFEM there is a penalty term scaled with  $\beta h^{-2}$ , hence in these methods we have the penalty parameter  $\beta$ . In TraceFEM we in addition have a stabilization term scaled by  $\beta' h^{-1}$ , hence in this method there is the stabilization parameter  $\beta'$ . In DI also a penalty term with a corresponding penalty parameter  $\beta$  occurs. A key parameter in this method is  $\epsilon > 0$ , which quantifies the interface thickness. The DI method also has a regularization term that contains the parameter  $\sigma$ . The specific parameter values that we use are given below in Section 4.

## 4 Numerical experiments

In this section we present results of a numerical experiment. We consider an  $n$ -tensor heat equation,  $n = 0, 1, 2$ , on a relatively simple surface consisting of a large flat part and a localized bump. The height of this bump is varied and the resulting surfaces have small negative and positive Gaussian curvature values in the bump region (for small bump height) and (very) large negative and positive Gaussian curvature values in the bump region (for larger bump height). The initial condition is essentially a regularized Dirac delta function with support disjoint from the bump support. In Section 4.1 we give a precise description of the problem setting. The four methods described in the sections above are applied to this model problem and some numerical results are presented. The numerical results illustrate that curvature can drastically affect the solution behavior.

Specific curvature related phenomena will be discussed in the Sections 4.2 – 4.4, for  $n = 0, 1, 2$ , respectively.

#### 4.1 Formulation of a tensor diffusion model problem

Let  $\mathcal{M}$  be the graph of a function  $f$ ,

$$\mathcal{M} = \{ \mathbf{x} = (\hat{x}^1, \hat{x}^2, f(\hat{x}^1, \hat{x}^2))^T \mid \hat{\mathbf{x}} = (\hat{x}^1, \hat{x}^2)^T \in \hat{\Omega} \subset \mathbb{R}^2 \}.$$

We want to study a flat surface with an isolated bump defining a region with negative and positive Gaussian curvature. The bump is described by  $f(\hat{\mathbf{x}}) := \alpha \eta(\|\hat{\mathbf{x}} - \hat{\mathbf{p}}\|/r)$ , with  $\alpha \geq 0$  a scaling factor,  $\hat{\mathbf{p}} \in \hat{\Omega}$  the center point of the bump, and  $r > 0$  its radius. The function  $\eta : \mathbb{R} \rightarrow \mathbb{R}$  represents a cut-off compressed Gaussian, i.e.,

$$\eta(d) = \eta(d; \delta) := \begin{cases} \exp\left(-\frac{1}{1-d^2}\right) & \text{if } d < 1 - \delta \\ 0 & \text{otherwise,} \end{cases}$$

with threshold value  $\delta = 0.025$ . See Figure 1 for a visualization of  $\mathcal{M}$ .

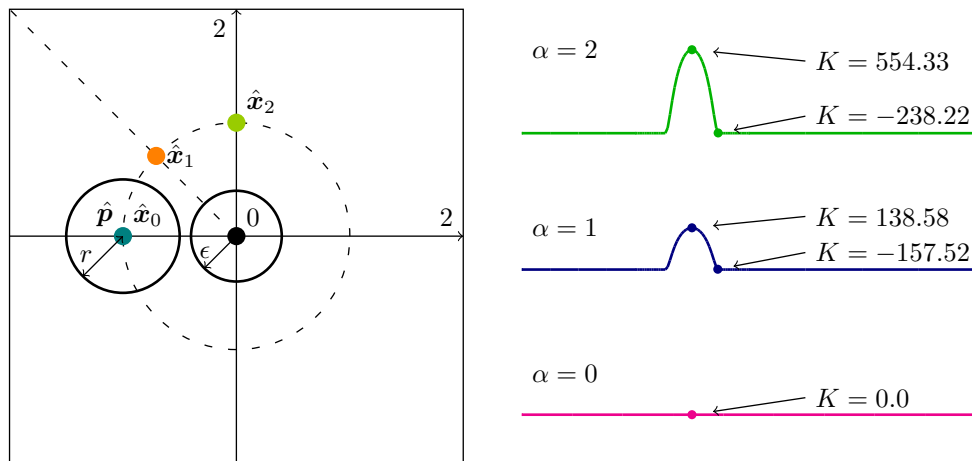


Figure 1: (Color online) Left: Sketch of the domain with origin colored in black, the outer radius of the bump centered at  $\hat{\mathbf{p}}$  with radius  $r$ , the initial solution radius  $\epsilon$ , and the three evaluation points  $\hat{\mathbf{x}}_0, \hat{\mathbf{x}}_1, \hat{\mathbf{x}}_2$  highlighted in three different colors. The overall domain size of  $\hat{\Omega}$  in the numerical computations is chosen to be  $[-2, 2]^2$ . Right: Plot of the bump surfaces along the  $\hat{x}_0$ -axis for  $\alpha \in \{0.0, 1.0, 2.0\}$ . Highlighted are the highest and lowest Gaussian curvature  $K$ .

Let  $\mathbf{p} \in \mathcal{M}$  represent a center point and  $\mathbf{u}_p \in \mathbb{T}_p^n \mathcal{M}$  a (tangential) tensor in  $\mathbf{p}$ , then we set as initial condition

$$\mathbf{u}^0(\mathbf{x}) = \delta_\epsilon(d_{\mathcal{M}}(\mathbf{x}, \mathbf{p})) \mathbf{u}_p, \text{ for } \mathbf{x} \in \mathcal{M},$$

with  $\delta_\epsilon(\cdot)$  the Dirac delta function. For simplicity we choose a point  $\mathbf{p}$  in a flat region away from the bump, so that  $d_{\mathcal{M}}(\mathbf{x}, \mathbf{p}) = \|\mathbf{x} - \mathbf{p}\|$ . The Dirac-delta function is

approximated by a single bump of radius  $\varepsilon$  around the origin, scaled by  $\varepsilon$ , such that  $\delta_\varepsilon(\|\mathbf{x}\|) = \varepsilon^{-2}\eta(\|\mathbf{x}\|/\varepsilon)$ .

We consider  $\hat{\mathbf{p}} = (-0.5, 0.0)^T$  and  $r = 0.25$  with varying  $\alpha \in [0.0, 2.0]$ . For the initial condition, we set  $\varepsilon = 0.2$  and

$$\mathbf{u}_p^{(0)} = 1, \quad \mathbf{u}_p^{(1)} = (-1, 0, 0)^T, \quad \mathbf{u}_p^{(2)} = \mathbf{u}_p^{(1)} \otimes \mathbf{u}_p^{(1)}$$

for the scalar, vector and tensor problem, respectively.

The heat equation is solved in the time interval  $t \in [0, 1]$  and on the surface  $\mathcal{M}$  with  $\hat{\Omega} = [-2, 2]^2$ . To illustrate the solution behavior we define three evaluation points in the parameter domain:  $\hat{\mathbf{x}}_0 = \hat{\mathbf{p}}$ ,  $\hat{\mathbf{x}}_1 = 0.25(-\sqrt{2}, \sqrt{2})^T$  and  $\hat{\mathbf{x}}_2 = (0.0, 0.5)^T$ , all on the circle with radius 0.5 around the origin in  $\hat{\Omega}$ , see Figure 1. For the evaluation of the (discrete) solution  $\mathbf{u}_h$ , these points need to be lifted to the discrete surface  $\mathcal{M}_h$ .

The discretization parameters are summarized in Table 1.

	$h$	$\Delta t$	$k$	$\beta$	$\beta'$	$\epsilon$	$\sigma$
Reference (SFEM)	0.0027	$10^{-4}$	2	10	—	—	—
ISFEM	0.011	$10^{-3}$	1	—	—	—	—
SFEM	0.011	$10^{-3}$	1	10	—	—	—
TraceFEM	0.0078	$10^{-3}$	1	0.01	1	—	—
DI	0.0156	$10^{-3}$	1	$10^3$	—	0.125	$10^{-8}$

Table 1: Numerical parameters used in the different methods. Note that for the TraceFEM and DI method, the grid size corresponds to the 3d element grid size. The polynomial order  $k$  represents the Lagrange polynomial order of the discrete function spaces.

With the parameters listed in the table all four methods determine approximate solutions within reasonable time on standard hardware.

Previous comparisons of the different methods have shown advantageous properties of SFEM with respect to accuracy and computational effort, see [3]. In order to provide numerical reference data, we use SFEM with a higher resolution in space and time and a higher polynomial order of the solution space. We set as finest space resolution on the bump the grid size  $h \approx 0.0027$ , timestep size  $\Delta t = 10^{-4}$ , and polynomial degree  $k = 2$ . In order to reduce the numerical influence of surface approximation, we have chosen  $\boldsymbol{\mu}_h \equiv \boldsymbol{\mu}$  for the SFEM reference computations.

## 4.2 Results for the scalar case

Starting from the initial delta peak at the origin, the scalar heat  $\mathbf{u}^{(0)}$  diffuses over the surface. In flat regions this diffusion is symmetric. For bump strength  $\alpha = 0$  this corresponds to the whole domain and thus the maximal heat remains on the initial position. Classical properties can be observed, as described already in Section 2.3. Not

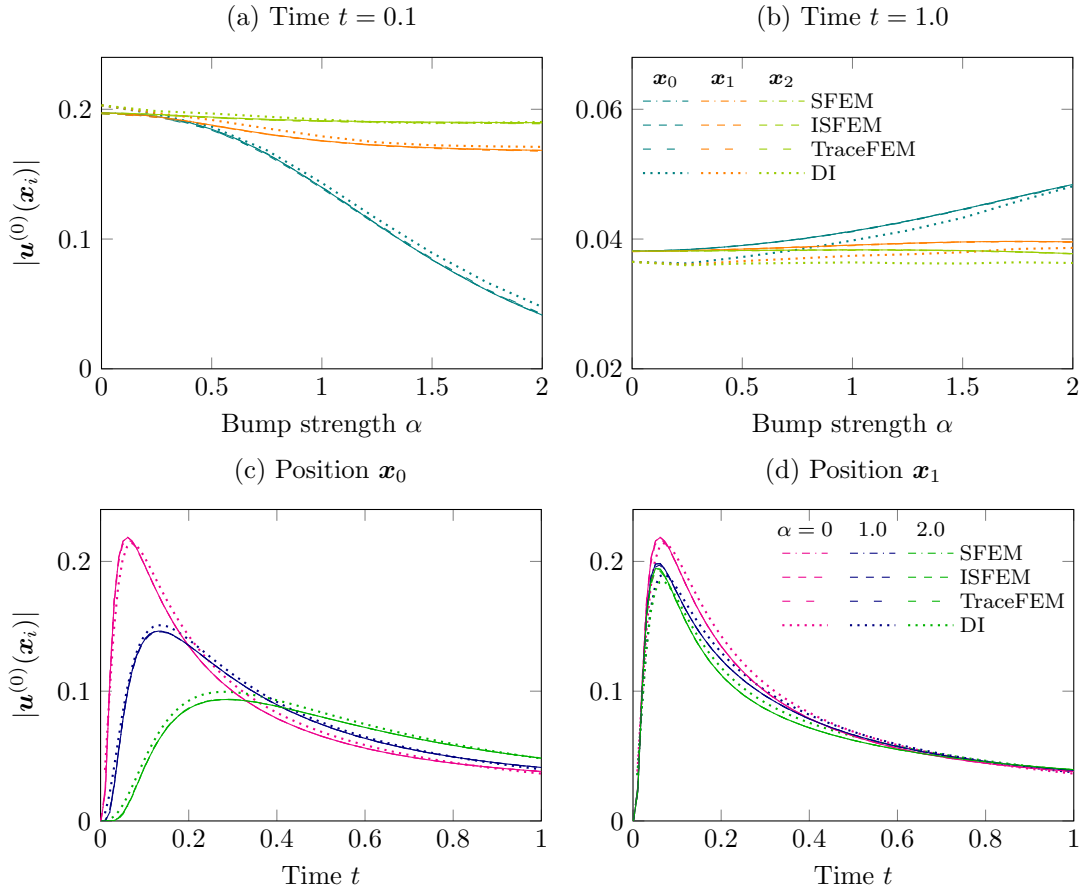


Figure 2: (Color online) Plot of scalar values  $|u^{(0)}(\mathbf{x}_i)|$  over  $\alpha$  (top) and over time  $t$  (bottom). Solid lines correspond to a reference solution. Colors correspond to  $\mathbf{x}_0$ ,  $\mathbf{x}_1$ , and  $\mathbf{x}_2$  and  $\alpha \in \{0.0, 1.0, 2.0\}$ .

surprisingly, with all four methods the flat case can equally well be represented, see Figure 2.

For  $\alpha > 0$ , the variation of the curvature introduces non-symmetric and anisotropic diffusion into the system. Figure 2 (top) shows that at early times,  $t = 0.1$ , when comparing the solution at the three points, the maximal heat value is at  $\mathbf{x}_2$ , while at  $t = 1.0$  this changes and the maximum value is at  $\mathbf{x}_0$  (on top of the bump). The difference between this maximum value at  $\mathbf{x}_0$  and the values at the other two points increases for larger  $\alpha$  values. Plotted over time in Figure 2 (bottom), there is a transition time point where the maximum changes. It can thus clearly be seen that the diffusion does not only depend on the geodesic distances on the surface but also on the surface curvature. The differences at  $\mathbf{x}_1$  and  $\mathbf{x}_2$ , points located in the flat region and having the same distance to the origin, also demonstrate that nearby curved regions influence the solution in the flat part. On curved surfaces the simple relation involving the (geodesic) distance only

holds for sufficiently short times. An explanation of the phenomenon observed in this experiment can be given using eq. (15). At the bottom of the bump, we have *negative* curvature, leading to *fast* diffusion around the bump, whereas in a small region that contains the bump center the *positive* curvature *slows down* the diffusion, leading to an accumulation of heat in the bump region. The heat diffuses out of the bump region when the difference between the heat values in this region and the region outside the bump is sufficiently large. These local differences also influence nearby regions with zero curvature.

The solution behavior is accurately resolved by all four numerical methods. The three consistent methods yield results that (in the “eye norm”) can hardly be distinguished from the reference solution, whereas the inconsistent DI method is less accurate (due to a too large  $\epsilon$  value).

### 4.3 Results for the vector case

For the vector case not only the norm but also the direction of  $\mathbf{u}^{(1)}$  is of interest. We thus measure at the three reference points the magnitude of the solution  $\|\mathbf{u}^{(1)}\|$  and the angle between the vector and the positive  $x^1$ -axis, i.e.,  $\angle(\mathbf{u}^{(1)}, \mathbf{e}_1) := \arccos \langle \mathbf{u}^{(1)} / \|\mathbf{u}^{(1)}\|, \mathbf{e}_1 \rangle$ , see Figure 3 and Figure 4, respectively.

At early times,  $t = 0.1$ , the norm behaves qualitatively similar to the scalar case, but at later times,  $t = 1.0$ , the behavior is very different. While scalar heat diffuses over the whole domain, in the vector case, the norm stays close to zero in the bump center for large  $\alpha$ , see Figure 3. It does not increase significantly over a very long time. In the scalar case with  $t = 1.0$  and  $\alpha \in [1, 2]$  we see that there is a distinct maximal heat value at the top of the bump, corresponding to  $\mathbf{x}_0$ , cf. Figure 2 (b). In the vector case with  $t = 1.0$  and  $\alpha \in [1, 2]$  the opposite happens: the norm values at the top of the bump are much smaller than in the other two points, cf. Figure 3 (b). It appears that there is a strong influence of the additional tangentiality constraint and of the interaction with the transport of the direction.

Figure 4 shows that the initial *direction*  $\mathbf{u}^0$  is instantaneously extended to the whole domain only in the case of  $\alpha = 0$ . For  $\alpha > 0$  this direction extension property only holds close to the origin. This coincides with the findings in [24] where the limit  $t \rightarrow 0$  is considered and a vector parallel transport is reconstructed from the vector heat flow solution. For larger times, the curvature of the surface causes a violation of this property. We see in Figure 4 (top) that even in the points in the flat region, i.e., in  $\mathbf{x}_1$  and  $\mathbf{x}_2$  with a flat geodesic to the origin, the ideal angle  $\pi$  is missed for  $\alpha > 0$ . Due to symmetry of the problem setup, on the bump,  $\mathbf{x}_0$ , the angle of the solution is the same as the initial angle. Note that due to the small vector norms on the bump, the evaluation of the angle is poorly conditioned and thus a small deviation from the  $x^1$ -axis, results in large deviations in the evaluated angle.

Interpreted as a minimization problem of the Dirichlet energy,  $\int_{\mathcal{M}} \|\nabla_{\mathcal{M}} \mathbf{u}\|^2 d\mathbf{x} \rightarrow \min$ , the vector heat equation minimizes gradients in the magnitude and gradients in the angle. For strongly curved domains, the (by curvature) enforced violation in the angle is compensated by reducing the norm of the vector. This has consequences and leads

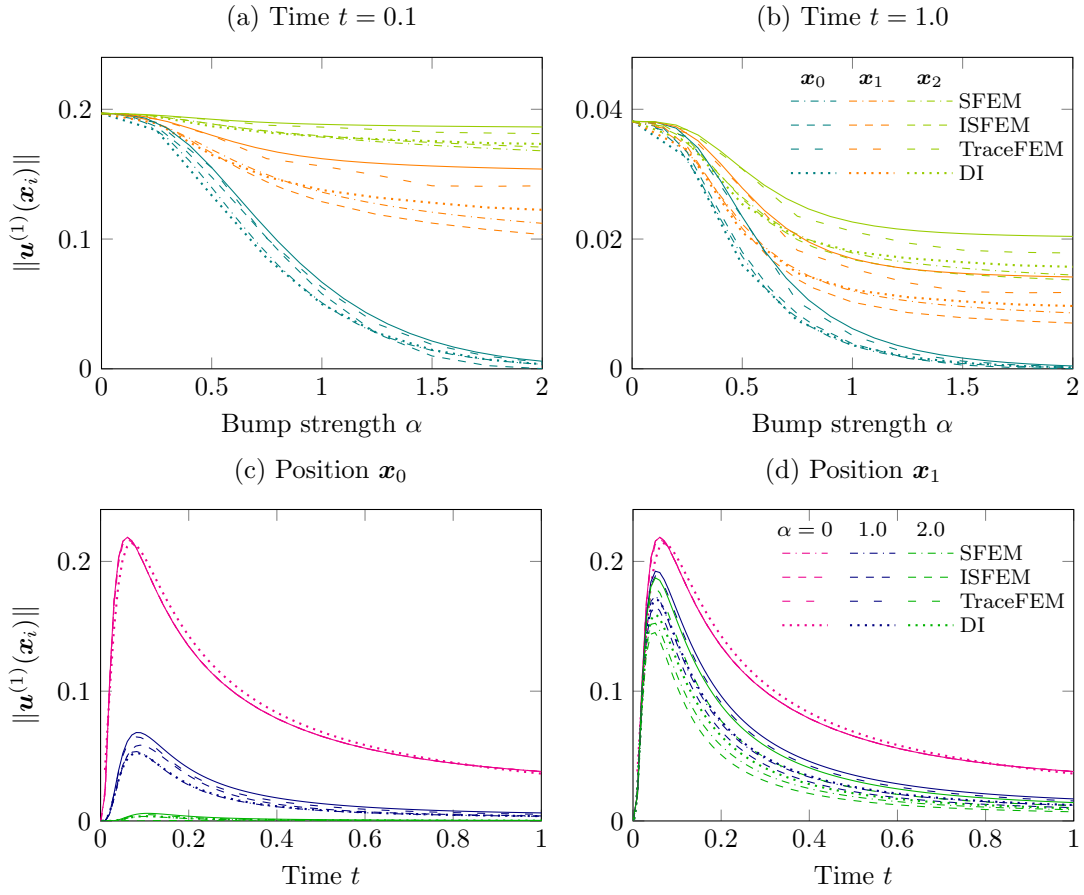


Figure 3: (Color online) Plot of the vector norm  $\|\mathbf{u}^{(1)}(\mathbf{x}_i)\|$  over  $\alpha$  (top) and over time  $t$  (bottom). Solid lines correspond to a reference solution. Colors correspond to  $\mathbf{x}_0$ ,  $\mathbf{x}_1$ , and  $\mathbf{x}_2$  and  $\alpha \in \{0.0, 1.0, 2.0\}$ .

to increased differences in the norm in the three reference points if compared with the scalar case.

All methods show qualitatively the same behavior. However, for all methods the differences with the reference solution are (significantly) larger compared with the scalar case. These differences increase for larger  $\alpha$  values. This loss of accuracy compared to the scalar case is caused by the significantly higher numerical problem complexity for  $n \geq 1$ , cf. discussion in Section 3.5. Depending on the method, the vector case requires the evaluation of derivatives of the projection (SFEM, TraceFEM, DI) or derivatives of the metric coefficients (ISFEM), and thus become more sensitive to the approximation of the geometry. This is also seen for the vector angle with large variations. These large variations are in addition due to the low evaluation accuracy in the point  $\mathbf{x}_0$  and the sensitivity of the evaluation to small perturbations.

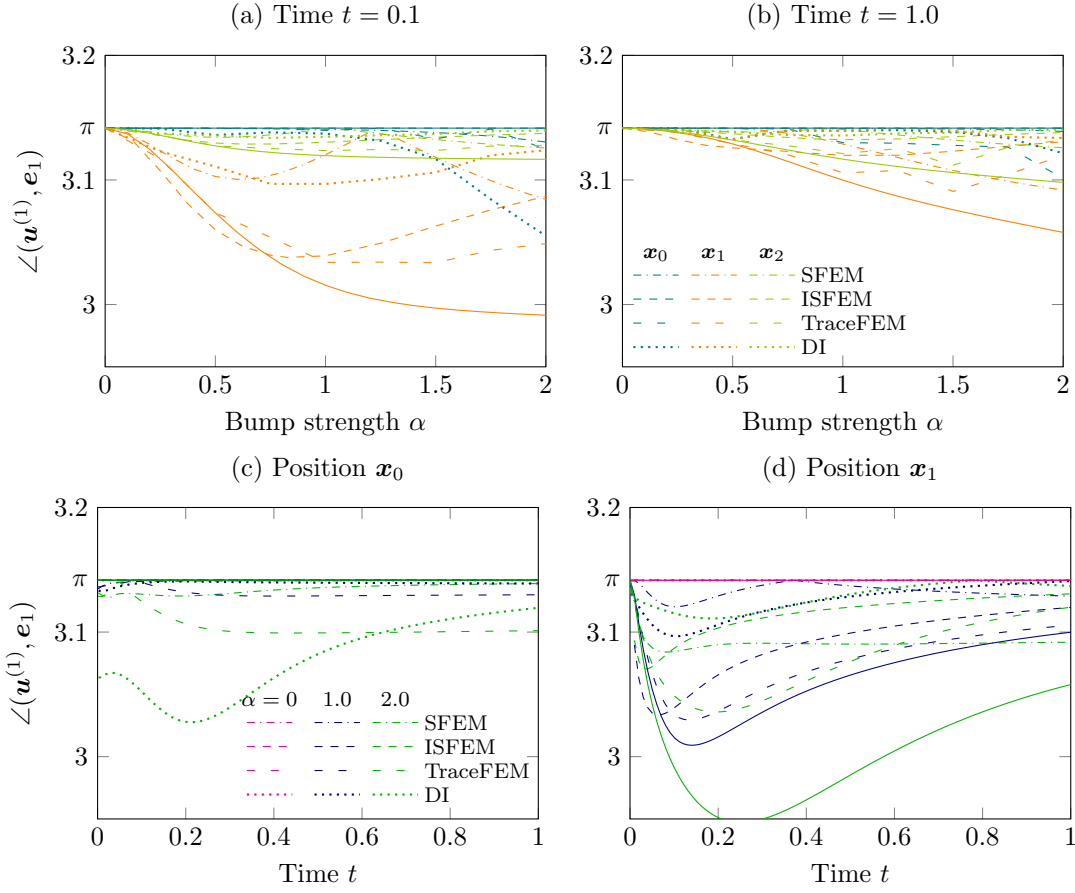


Figure 4: (Color online) Plot of the angle between the vector  $\mathbf{u}^{(1)}(\mathbf{x}_i)$  and the positive  $x$ -axis  $\mathbf{e}_1 = (1, 0, 0)^T$  over  $\alpha$  (top) and over time  $t$  (bottom). Solid lines correspond to a reference solution. Colors correspond to  $\mathbf{x}_0, \mathbf{x}_1$ , and  $\mathbf{x}_2$  and  $\alpha \in \{0.0, 1.0, 2.0\}$ .

#### 4.4 Results for the tensor case

For the tensor case we again consider the norm  $\|\mathbf{u}^{(2)}\|$  and the angle with the positive  $x^1$ -axis. The tensor angle is defined as follows:  $\angle(\mathbf{u}^{(2)}, \mathbf{e}_1) := \arccos \langle \mathbf{u}^{(2)} / \|\mathbf{u}^{(2)}\|, \mathbf{e}_1 \otimes \mathbf{e}_1 \rangle$ . We again measure these quantities at the three reference points. Due to the increased complexity we here only show results for SFEM and DI, without the corresponding reference solution, see Figure 5 and Figure 6, respectively. The results are qualitatively similar to the vector case and can be explained by the same reasoning.

The qualitative behavior can be resolved by both methods. However, the differences between the methods further increase.

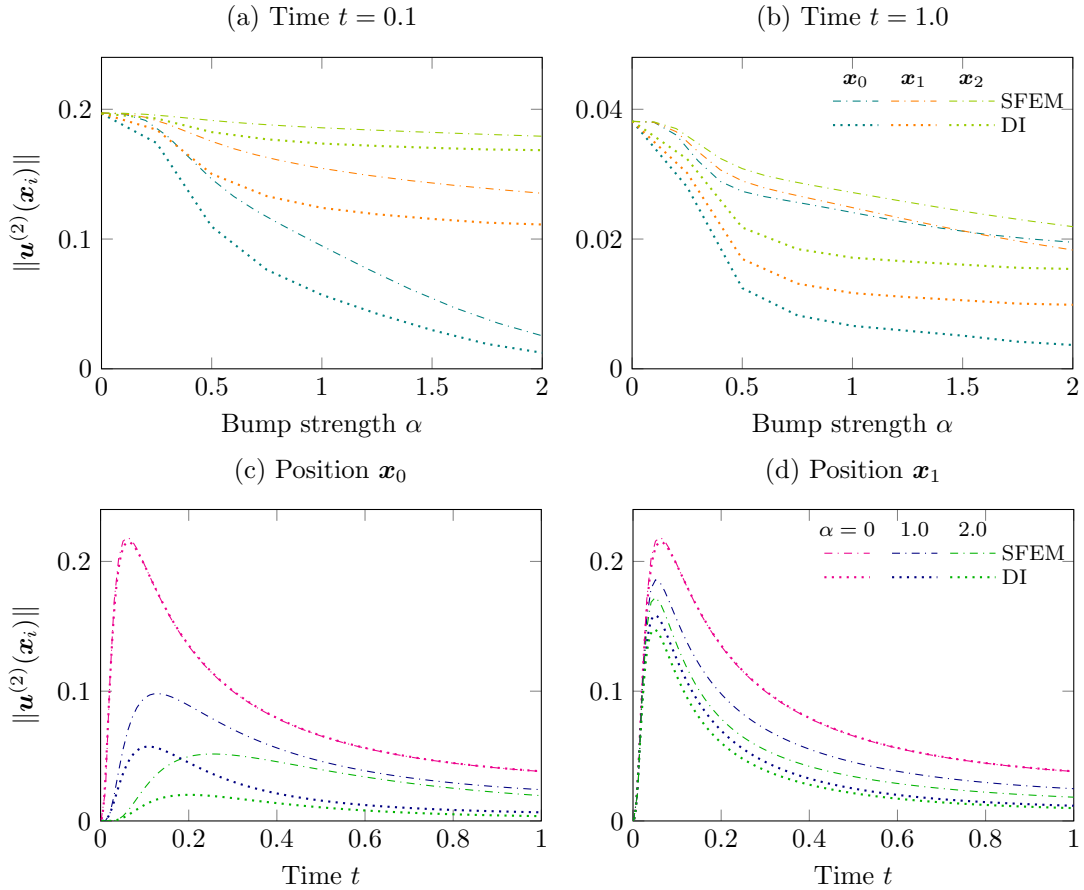


Figure 5: (Color online) Plot of the tensor norm  $\|\mathbf{u}^{(2)}(\mathbf{x}_i)\|$  over  $\alpha$  (top) and over time  $t$  (bottom). Solid lines correspond to a reference solution. Colors correspond to  $\mathbf{x}_0$ ,  $\mathbf{x}_1$ , and  $\mathbf{x}_2$  and  $\alpha \in \{0.0, 1.0, 2.0\}$ .

## 4.5 Summary

While some analytical results exist for the diffusion of tangential tensor fields, see Section 2.3, quantitative results which allow to test numerical algorithms on simple benchmark problems have been missing. We here provided such a setup. We have considered four different numerical methods, ISFEM, SFEM, TraceFEM, and DI, all based on finite element discretizations. They are briefly described and compared with each other. The methods differ with respect to the surface representation, the representation of the gradient operator and the geometric information, and the tangentiality condition. The methods were applied to a benchmark problem with a relatively simple surface geometry. We observe that for not too small curvature values the solution behavior is strongly influenced by the geometry. Furthermore, the results show a stronger coupling with geometric properties and an increased sensitivity on the resolution of these properties for increased tensor degree. Due to this, there is a significant increase in numerical



complexity when going from tensor degree  $n = 0$  to  $n \geq 1$ .

A wealth of applications exists in materials science and biology, which make use of the influence of curvature of thin structure. Modeling such effects often requires tangential vector or tensor fields. We suggest to first test numerical methods for such applications on the provided setup, to ensure a proper resolution of the geometric influence.

**Acknowledgment** The authors wish to thank the German Research Foundation (DFG) for financial support within the Research Unit “Vector- and Tensor-Valued Surface PDEs” (FOR 3013) with project no. RE 1461/11-1 and VO 899/22-1. We further acknowledge computing resources provided by ZIH at TU Dresden and within project PFAMDIS at FZ Jülich.

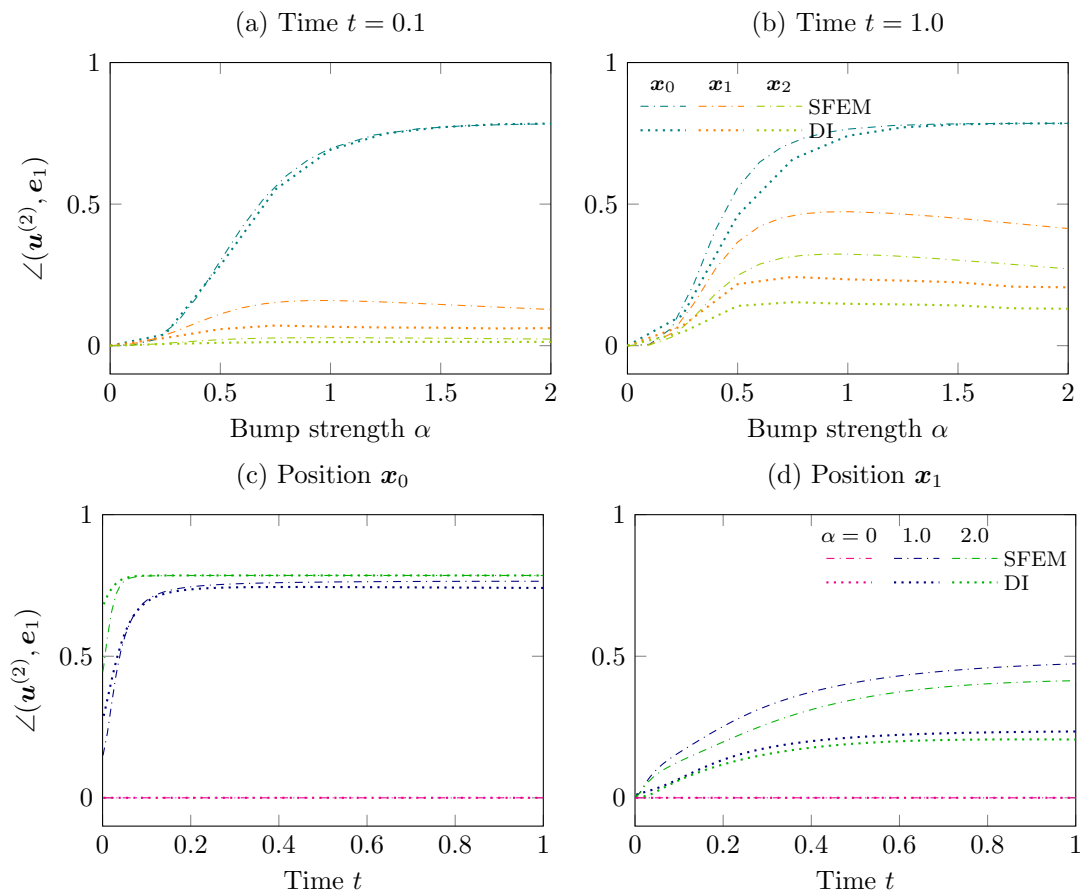


Figure 6: (Color online) Plot of the angle between the tensor  $\mathbf{u}^{(2)}(\mathbf{x}_i)$  and the positive  $x$ -axis  $\mathbf{e}_1 = (1, 0, 0)^T$  over  $\alpha$  (top) and over time  $t$  (bottom). Solid lines correspond to a reference solution. Colors correspond to  $\mathbf{x}_0, \mathbf{x}_1$ , and  $\mathbf{x}_2$  and  $\alpha \in \{0.0, 1.0, 2.0\}$ .

## References

- [1] E. Bachini, M. W. Farthing, and M. Putti. Intrinsic finite element method for advection-diffusion-reaction equations on surfaces. *J. Comput. Phys.*, 424:109827, 2021. doi:[10.1016/j.jcp.2020.109827](https://doi.org/10.1016/j.jcp.2020.109827).
- [2] A. Bonito, A. Demlow, and R. H. Nochetto. Chapter 1 - Finite element methods for the Laplace–Beltrami operator. In A. Bonito and R. H. Nochetto, editors, *Geometric Partial Differential Equations - Part I*, volume 21 of *Handbook of Numerical Analysis*, pages 1–103. Elsevier, 2020. doi:[10.1016/bs.hna.2019.06.002](https://doi.org/10.1016/bs.hna.2019.06.002).
- [3] P. Brandner, T. Jankuhn, S. Praetorius, A. Reusken, and A. Voigt. Finite element discretization methods for velocity-pressure and stream function formulations of surface Stokes equations. *SIAM J. Sci. Comput.*, 2022. doi:[10.1137/21M1403126](https://doi.org/10.1137/21M1403126). arXiv:[2103.03843](https://arxiv.org/abs/2103.03843). (in press).
- [4] F. Bürger. *Interaction of mean curvature flow and a diffusion equation*. PhD thesis, Universität Regensburg, 2021.
- [5] E. Burman, P. Hansbo, M. G. Larson, and A. Massing. Cut finite element methods for partial differential equations on embedded manifolds of arbitrary codimensions. *ESAIM: M2AN*, 52(6):2247–2282, 2018. doi:[10.1051/m2an/2018038](https://doi.org/10.1051/m2an/2018038).
- [6] C. G. Claudel and A. M. Bayen. Lax–hopf based incorporation of internal boundary conditions into Hamilton–Jacobi equation. Part II: computational methods. *IEEE Trans. Automat. Contr.*, 55(5):1158–1174, 2010. doi:[10.1109/TAC.2010.2045439](https://doi.org/10.1109/TAC.2010.2045439).
- [7] K. Crane, C. Weischedel, and M. Wardetzky. Geodesics in heat: a new approach to computing distance based on heat flow. *ACM Trans. Graph.*, 32(5):1–11, 2013. doi:[10.1145/2516971.2516977](https://doi.org/10.1145/2516971.2516977).
- [8] A. Demlow. Higher-order finite element methods and pointwise error estimates for elliptic problems on surfaces. *SIAM J. Numer. Anal.*, 47(2):805–827, 2009. doi:[10.1137/070708135](https://doi.org/10.1137/070708135).
- [9] G. Dziuk and C. M. Elliott. Finite element methods for surface PDEs. *Acta Numer.*, 22:289–396, 2013. doi:[10.1017/s0962492913000056](https://doi.org/10.1017/s0962492913000056).
- [10] J. Faraudo. Diffusion equation on curved surfaces. i. theory and application to biological membranes. *J. Chem. Phys.*, 116(13):5831–5841, 2002. doi:[10.1063/1.1456024](https://doi.org/10.1063/1.1456024).
- [11] J. Grande, C. Lehrenfeld, and A. Reusken. Analysis of a high-order trace finite element method for PDEs on level set surfaces. *SIAM J. Numer. Anal.*, 56(1):228–255, 2018. doi:[10.1137/16m1102203](https://doi.org/10.1137/16m1102203).
- [12] H. P. McKean, Jr. and I. M. Singer. Curvature and the eigenvalues of the Laplacian. *J. Differ. Geom.*, 1(1–2):43–69, 1967. doi:[10.4310/jdg/1214427880](https://doi.org/10.4310/jdg/1214427880).

- [13] P. Hansbo, M. G. Larson, and K. Larsson. Analysis of finite element methods for vector Laplacians on surfaces. *IMA J. Numer. Anal.*, 40(3):1652–1701, 2020. doi:[10.1093/imanum/drz018](https://doi.org/10.1093/imanum/drz018).
- [14] H. Hardering and S. Praetorius. Tangential errors of tensor surface finite elements. *IMA J. Numer. Anal.*, page drac015, 2021. doi:[10.1093/imanum/drac015](https://doi.org/10.1093/imanum/drac015).
- [15] T. Jankuhn and A. Reusken. Trace finite element methods for surface vector-Laplace equations. *IMA J. Numer. Anal.*, 41(1):48–83, 2020. doi:[10.1093/imanum/drz062](https://doi.org/10.1093/imanum/drz062).
- [16] F. Knöppel, K. Crane, U. Pinkall, and P. Schröder. Globally optimal direction fields. *ACM Trans. Graphics*, 32(4):1–10, 2013. doi:[10.1145/2461912.2462005](https://doi.org/10.1145/2461912.2462005).
- [17] C. Lehrenfeld and A. Reusken. High order unfitted finite element methods for interface problems and PDEs on surfaces. In D. Bothe and A. Reusken, editors, *Transport Processes at Fluidic Interfaces*, pages 33–63. Birkhäuser, Cham, 2017. doi:[10.1007/978-3-319-56602-3\\_2](https://doi.org/10.1007/978-3-319-56602-3_2).
- [18] X. Li, J. Lowengrub, K. E. Teigen, A. Voigt, and F. Wang. A diffuse-interface approach for modelling transport, diffusion and adsorption/desorption of material quantities on a deformable interface. *Commun. Math. Sci.*, 7(4):1009–1037, 2009. doi:[10.4310/cms.2009.v7.n4.a10](https://doi.org/10.4310/cms.2009.v7.n4.a10).
- [19] C. Lubich, D. Mansour, and C. Venkataraman. Backward difference time discretization of parabolic differential equations on evolving surfaces. *IMA J. Numer. Anal.*, 33(4):1365–1385, 2013. doi:[10.1093/imanum/drs044](https://doi.org/10.1093/imanum/drs044).
- [20] M. Nestler, I. Nitschke, S. Praetorius, and A. Voigt. Orientational order on surfaces: the coupling of topology, geometry, and dynamics. *J. Nonlinear Sci.*, 28:147–191, 2018. doi:[10.1007/s00332-017-9405-2](https://doi.org/10.1007/s00332-017-9405-2).
- [21] M. Nestler, I. Nitschke, and A. Voigt. A finite element approach for vector- and tensor-valued surface PDEs. *J. Comput. Phys.*, 389:48–61, 2019. doi:[10.1016/j.jcp.2019.03.006](https://doi.org/10.1016/j.jcp.2019.03.006).
- [22] M. A. Olshanskii and A. Reusken. Trace finite element methods for PDEs on surfaces. In S. P. A. Bordas, E. Burman, M. G. Larson, and M. A. Olshanskii, editors, *Geometrically Unfitted Finite Element Methods and Applications*, pages 211–258. Springer, Cham, 2017.
- [23] A. Rätz and A. Voigt. PDE’s on surfaces — A diffuse interface approach. *Commun. Math. Sci.*, 4(3):575–590, 2006. doi:[10.4310/CMS.2006.v4.n3.a5](https://doi.org/10.4310/CMS.2006.v4.n3.a5).
- [24] N. Sharp, Y. Soliman, and K. Crane. The vector heat method. *ACM Trans. Graph.*, 38(3):1–19, 2019. doi:[10.1145/3243651](https://doi.org/10.1145/3243651).
- [25] A. Singer and H.-T. Wu. Vector diffusion maps and the connection Laplacian. *Commun. Pure Appl. Math.*, 65(8):1067–1144, 2012. doi:[10.1002/cpa.21395](https://doi.org/10.1002/cpa.21395).

- [26] F. Stenger. Meshconv: a tool for various mesh-conversions and mesh-transformations. <https://gitlab.mn.tu-dresden.de/iwr/meshconv>, 2020. v3.20.
- [27] J. Sun, M. Ovsjanikov, and L. Guibas. A concise and provably informative multi-scale signature based on heat diffusion. In *Proc. Symp. Geom. Process. '09*, pages 1383–1392, Goslar, DEU, 2009. Eurographics Association. doi:[10.5555/1735603.1735621](https://doi.org/10.5555/1735603.1735621).
- [28] S. R. S. Varadhan. On the behavior of the fundamental solution of the heat equation with variable coefficients. *Commun. Pure Appl. Math.*, 20(2):431–455, 1967. doi:[10.1002/cpa.3160200210](https://doi.org/10.1002/cpa.3160200210).
- [29] S. Vey and A. Voigt. AMDiS: adaptive multidimensional simulations. *Comput. Vis. Sci.*, 10(1):57–67, 2006. doi:[10.1007/s00791-006-0048-3](https://doi.org/10.1007/s00791-006-0048-3).